Modeling of rheological and electro-chemical properties of hydrated clays

Maxim G. KHRAMCHENKOV ▪ Kazan Federal University ▪ mkhramch@gmail.com
Rustem M. USMANOV ▪ Kazan Federal University

Érkezett: 2017. 10. 11. ▪ Received: 11. 10. 2017. ▪ https://doi.org/10.14382/epitoanyag-jsbcm.2017.19

Abstract

A unite mathematical model of rheological and electro-chemical properties of saturated clays is proposed. The foundation of the model is the unification of filtration's consolidation theory, the theory of stability of lyophobic colloids and the experimental data on electro-chemical properties of clays and clayey suspensions. Conception of disjoining pressure as a surplus in comparison with hydraulic plays the important role in clays properties description. This pressure is caused by surface capacities and exists in water films between clay particles. We obtained the exact solution about wringing the water out of clay layer. The solution that we received not demands to introduce a concept of limit shear stress for clays. We investigate the peculiarities of the model, which are important for explaining some character features of electro- and mass-transfer processes in clays with coupling of rheological behavior of clays. It is shown that solutions which we've received are in good harmony with results of experiments.

Keywords: kaolinite, montmorillonite, modelling, viscosity, electro-conductivity
Kulcsszavak: kaolinit, montmorillonit, modellezé, viszkozitás, elektromos vezetőképesség

Prof. Maxim G. KHRAMCHENKOV
Director of Institute of Mathematics and Mechanics of the Kazan Federal University. Scientific Degree: Dr. Science in Mathematical Simulation. Scientific Interest: Thermal, hydraulic, mechanical and chemical processes in geosystems and engineering.

Rustem M. USMANOV
Postgraduate student at Institute of Geology and Oil and Gas Technologies of the Kazan Federal University.

1. Introduction

The specific properties of clays and their compositions (low permeability and thermo-conductivity, plasticity in moist condition) are caused by existence of specific particles and their compositions-clay minerals. Clay minerals are hydro-alumosilicates of calcium, sodium, potassium and they often are structurally arranged like thin sheet particles (about 50-100nm in diameter and 1nm in height) [1]. Generally speaking, particles of clay minerals have the appearance of thin isometric or elongated plates, scales, needles and tubes.

Before we proceed to theoretical examination of electro-chemical and rheological properties of clays, we describe the simplest structure of clay sample or clayey rock. We will consider clays like solid porous skeleton (not essential coherent), which pores can change own size and form during swelling of clay minerals. After the filling of all pore volume by swelled clay, the process of total sample or rock swelling is started. In that case any process, connected with deformation of clays, could be described like:

1. Electro-chemical process in pores (part of medium volume, which is filled by clay particles, and their interlayer intervals).
2. Mechanical processes, connected with deformation of hard particles and dynamics of water films between them.

It is very important that their two processes are always conducted instantaneously. After solution of mass and energy balance equations for liquid and solid phase we obtain the equations for description of rheology and mass transport processes in clays [2]. On the first stage of deformation, until the full disappearing of transport pores, water in interlayer between clay particles doesn't perceive the effective tensions of skeleton [3] and it is in thermodynamic equilibrium [4–8] with water in transport pores, so it satisfies the equation that disjoining pressure is zero. This fact means that the volume which is filled with clay particles and interlayer water, reserves. On the second stage free porosity is zero and we will have to specify the law of filtration in such a system (on the first stage we supposed that filtration velocity $\vec{q}$ satisfies the law of Darcy) In this case we will have a contribution of disjoining pressure to free energy of system. In the moment disjoining pressure is able to give an addition to hydraulic pressure, in dependence of the value of dilation. This fact can explain the nature of anomalous high seam pressures in deep-laying clay-containing reservoirs. Also the electro-chemical effects give impact in rheological behavior of clays.

2. Mechanics of clays and clayey rocks

The specific properties of clay rocks (low permeability, plasticity in moist condition) are caused by existence of clay minerals in their composition. Because of isomorphic replacement in crystal matrix this particles usual carry electrical charge (usually negative), which is compensated by cations. Cations are adsorbed on to the surface of particles and at hydration they are able to dissociate (totally or partly) and make the double diffusion layer [1, 2]. As already it has been told above, any process, connected with deformation of clay rocks, could be divide in two stages: 1) free (transport) porosity (part of pore volume, which is not filled by clay particles and their interlayer intervals) is not equal zero; 2) free (transport) porosity is equal zero, it means that all pores are filled by clay particles and interlayer films of water. We begin examination from the first stage. We will consider that the filtration is going only in free part of pores. Now we can write mass balance equations for liquid and solid phase:

$$\frac{\partial(m_{p,c}\rho_f)}{\partial t} + \mathrm{div}(\rho_f m_{p,c}\vec{V}_{f,c}) \pm j = 0, \qquad (1)$$

$$\frac{\partial\left[(1-m_p-m_c)\rho_s\right]}{\partial t}+\mathrm{div}[\rho_s(1-m_p-m_c)\overrightarrow{V_s}]=0 \qquad (2)$$

In this equations ρ_f is a density of fluid (water), ρ_s – density of solid phase, $\overrightarrow{V_f}$ – fluid velocity in transport pores, $\overrightarrow{V_c}$ – fluid velocity between clay particles, $\overrightarrow{V_s}$ – solid phase velocity, m_p – free (transport) porosity, m_c – part of interlayer water in volume (internal porosity of clay minerals), j – water exchanging flow in the system «transport pores – water between clay particles». We assume that ρ_f and ρ_s are constants. Then after adding (1) and (2), and after accounting $\mathrm{div}\overrightarrow{V_s}=\partial\theta/\partial t=\dot{\theta}$, $\mathrm{div}[m_p(\overrightarrow{V_f}-\overrightarrow{V_s})]=\vec{q}$, we receive the equation

$$\dot{\theta}+\mathrm{div}\vec{q}=0, \qquad (3)$$

where we adopt that $\overrightarrow{V_c}=\overrightarrow{V_s}$ for clay particles (it means that filtration of water in water films between of clay particles is absent). Here θ is dilation (shrinkage in the case of consolidation), $\vec{q}$ – filtration velocity. Now we write conditions of mechanical balance. We suppose that an external load G is exerted to clay. Then the distribution of load between the rock components gives an equation

$$G_{ij}=(1-m_p-m_c)\sigma_{ij}-m_c(p+\Pi)\delta_{ij}-m_p p\delta_{ij}, \qquad (4)$$

which after the designation

$$(1-m_p-m_c)(\sigma_{ij}+p\delta_{ij})=\sigma_{ij}^f \qquad (5)$$

can be written in such a form

$$G_{ij}=\sigma_{ij}^f-m_c\Pi\delta_{ij}-p\delta_{ij}. \qquad (6)$$

In this equations p – pressure in liquid, Π – disjoining (additional to hydraulic) pressure in water interlayer films between clay particles, the aim of introduction of the σ_{ij}^f will be explained below. Now proceed to thermodynamic balance. Denote free energy of solid phase through macro-parameters σ^f, m_p, m_c, θ, Π. For this purpose we will write first and second law of thermodynamic for solid phase

$$\mathrm{d}U_s=\delta Q^{(e)}+\delta A^{(i)}+\delta A^{(e)}, T\,\mathrm{d}S_s=\delta Q^{(e)}+\delta Q'. \qquad (7)$$

Here U_s is an internal energy of skeleton, S_s – entropy of solid phase, $\delta Q^{(e)}$ – external stream of heat, $\delta Q'\geq 0$ - summary internal stream of heat (dissipation energy function), $\delta A^{(i)}$ - elementary mechanical work of internal surface strength. We will assume that in our case $\delta A^{(i)}$ is caused by transformation of part of total deformation energy in deformation of solid particles, and $\delta A^{(e)}$ is caused mainly by transformation of part of total deformation energy in a work on the displacement of particle with electrical charge. In isothermal conditions

$$\delta A^{(i)}+\delta A^{(e)}=\mathrm{d}U_s-T\,\mathrm{d}S_s+\delta Q'=\mathrm{d}F_s+\delta Q'. \qquad (8)$$

Let's examine mechanical properties of solid phase. Then in conditions of absence of mass forces we have the equation

$$\frac{\delta A^{(i)}}{\mathrm{dt}}=\int_{V_s}\sigma_{ij}^s\frac{\partial u_i}{\partial x_j}\mathrm{dV}=\int_{V_s}\frac{\partial\sigma_{ij}^s u_i}{\partial x_i}\mathrm{dV}, \qquad (9)$$

where u_i is a component of the vector of transference velocity of skeleton's particles, σ_{ij}^s is a skeleton's stresses. After transformation volume integral into surface integral we obtain:

$$\frac{\delta A^{(i)}}{\mathrm{dt}}=\int_{V_0}\frac{\partial(\sigma_{ij}^f\langle u_i\rangle)}{\partial x_i}\mathrm{dV}_0+(-p)\int_{\sum_s}u_i n_i\,\mathrm{d}s+(-\Pi)\int_{S_{S-C}}u_i n_i\,\mathrm{d}s, \qquad (10)$$

where $\sigma_{ij}^f=(1-m_p-m_c)(\langle i_{ij}^s\rangle-\langle\sigma-p\rangle\delta_{ij})$ is a tensor of effective tensions, corresponding to eq. (4), $\sigma=-(1/3)\sigma_{ii}^s$ is the pressure in the solid phase, i_{ij}^s is a deviator of the σ_{ii}^s. It is clear that

$$\int_{\sum_s}u_i n_i\,\mathrm{d}S=\dot{V}_s$$

is the velocity of changing of the solid phase volume.

Taking into account that in our case

$$\delta A^{(e)}/dt=\int_{V_c}\varphi\cdot dE/dt\,,$$

where φ – electrical potential in the volume near clay particle, E – volume density of electrical charge of clay particles, and both value φ, E are functions of the displacement of clay particles and depend from deformation's velocity tensor, we will use Ohm law $\varphi-\varphi_0=\kappa^{-1}j$, $dE/dt=j$, and also we will assume that $j=\gamma_{ij}e_{ij}$, so for member $\varphi dE/dt$ we have $\varphi dE/dt=(\gamma_{ij}\gamma_{ij})^2\cdot\kappa^{-1}(\dot{\theta})^2+\kappa^{-1}(\gamma_{ij}e'_{ij})^2+\gamma_{ij}\cdot\varphi_0 e_{ij}$. Here e_{ij} is a tensor of deformation's velocities, e'_{ij} is a deviator of the tensor of deformation's velocities, γ_{ij} – tensor of structural characteristics of clay particle arrangement, κ – electro-conductivity of water film, φ_0 – electrical potential in the middle part of clayey pores.

During the first stage of deformation, until the full disappearing of transport pores, water in interlayer between clay particles doesn't perceive the effective tensions of skeleton and it is in thermodynamic balance with water in transport pores, so it satisfies the equation Π=0. So in during of the first stage from the condition $\rho_s V_s=M_s$, $M_s=\mathrm{const}$ we receive

$$\frac{1}{V_0}\left(\dot{F}_s+\frac{\delta Q'}{\mathrm{dt}}\right)=\sigma_{ij}^f e_{ij}+\frac{(1-m_p-m_c)}{\rho_s}\dot{\rho}_s p+[(\gamma_{ij}\gamma_{ij})^2\cdot\kappa^{-1}(\dot{\theta})^2+\kappa^{-1}(\gamma_{ij}e'_{ij})^2+\varphi_0\cdot(\gamma_{ij}e_{ij})] \qquad (11)$$

For the case of elastic solid material $\delta Q'/\mathrm{dt}=0$. Then from the last equation we receive that

$$\dot{F}_s=T_{ij}e'_{ij}-\sigma^f\dot{\theta}+(1-m_p-m_c)p\frac{\dot{\rho}_s}{\rho_s}+[(\gamma_{ij}\gamma_{ij})^2\cdot\kappa^{-1}(\dot{\theta})^2+\kappa^{-1}(\gamma_{ij}e'_{ij})^2+\varphi_0\cdot(\gamma_{ij}e_{ij})] \qquad (12)$$

So far as disjoining pressure Π is a function of thickness of water interlayer h between clay particles, that's why condition Π=0 is equivalent to condition h = const. This means that the volume which is filled with clay particles and interlayer water V_c preserves. Let's write it as $m_c V_0=V_c$, V_c = const. Then from the last equation we obtain: $\dot{m}_c/m_c=-\dot{V}_0/V_0=-\dot{\theta}$, so

$$m_c=m_c^{(0)}\exp(-\theta). \qquad (13)$$

Because $(1-m_p-m_c)\rho_s V_0=M_s$=const, then

$$\frac{\mathrm{d}[\ln V_0+\ln\rho_s+\ln(1-m_p-m_c)]}{\mathrm{dt}}=0, \qquad (14)$$

and we'll receive one equation for three variables. In the most simple case, when ρ_s=const it can be written in such a form

$$\frac{1-m_p^{(0)}-m_c^{(0)}}{1-m_p-m_c}=1+\theta. \qquad (15)$$

Then for the free energy we have a dependences $F_S = F(J_2', \theta, \rho_S)$, where J_2' – is the second invariant of the tensor of deformations, then

$$\dot{F}_s = \frac{\partial F}{\partial J_2'}\varepsilon_{ij}' e_{ij}' + \frac{\partial F}{\partial \theta}\dot{\theta} + \frac{\partial F}{\partial \rho_s}\dot{\rho}_s.$$

Comparing right parts of equations for the $\dot{F}_s$ gives for concrete view of the F for the elastic skeleton [8] $F = \frac{\lambda}{2}\theta^2 + \mu J_2' - \upsilon\theta\sqrt{J_2'}$, where λ, μ, υ = const, next correlation

$$-\sigma^f - (\gamma_{ij}\gamma_{ij})^2 \cdot \kappa^{-1}\dot{\theta} = \lambda\theta - \nu\sqrt{J_2'},$$

$$(T_{ij} + \varphi_0 \cdot \gamma_{ij}) - (\gamma_{ij}\gamma_{ij})^2 \cdot \kappa^{-1} e_{ij}' = (2\mu - \nu\theta/\sqrt{J_2'})\varepsilon_{ij}' \qquad (16)$$

Last equations play roles of rheological correlations. They give us an ability to get closed system of equations for filtration consolidation of clays on the first stage. On the second stage m = 0, and we have to specify the law of the filtration in such a system, because we have ignored the filtration of water between clay particles till this moment (on the first stage we consider that for the $\vec{q}$ the law of Darcy [8] is carry out). Let's use the correlation for case m_p = 0:

$$m_c = \beta - (1-\beta)\theta, \quad \beta = m_c^{(0)} + m_p^{(0)}, \qquad (17)$$

so $\dot{m}_c = -(1-\beta)\dot{\theta}$. In this case we must take into account the last term of (10). This item describes the pressure of water between clay particles,

$$\Pi \int_{S_{s-c}} u_i n_i \, dS / V_0 = -\Pi \dot{V}_c / V_0 = -\Pi(\dot{m}_c + \dot{\theta} m_c) \qquad (18)$$

Then for the elastic pore environment we have analogically in this case

$$-\sigma^f - [m_c - (1-\beta)]\Pi - (\gamma_{ij}\gamma_{ij})^2 \cdot \kappa^{-1}\dot{\theta} = \lambda\theta - \nu\sqrt{J_2'},$$

$$(T_{ij} + \varphi_0 \cdot \gamma_{ij}) - (\gamma_{ij}\gamma_{ij})^2 \cdot \kappa^{-1} e_{ij}' = (2\mu - \nu\theta/\sqrt{J_2'})\varepsilon_{ij}' \qquad (19)$$

As far as in the first equation there is a term which contains the disjoining pressure which itself depends on the thickness of interlayer film of water h, it's necessary to determine the form of function $h(\theta)$, that is to say to connect micro-parameter h with macro-variables of process. From one side we have the correlation (15) for m_c and from another side $m_c = S_c h / V_0, S_c = \text{const}$. Here S_c is a half-square of the surface of clay particles which are situated in the volume V_0. Let's differentiate the left and right part of the last correlation with respect to time, so we receive

$$h = \frac{h^{(1)}}{m^{(1)}}[\beta - (1-\beta)\theta]\exp(\theta). \qquad (20)$$

Here $h^{(1)}, m_c^{(1)}$ – constants, which provides connection of the first and second stages. The last correlation will become more physical clear if we recall that shrinkage θ<0. So process of consolidation of clay rocks on the second stage determines the value h and, consequently the disjoining pressure as a function of macro-variable θ. In the moment disjoining pressure is able to give an addition to hydraulic pressure, in dependence of the value of θ. This fact can explain the nature of anomalous high seam pressures in deep-laying clay-containing reservoirs.

3. Rheological and electro-chemical properties of clays

Let's analyze the solution of second equation of (19). In the case of pure shift this solution has a simple view

$$\varepsilon_{ij}' = \frac{(T_{ij} + \varphi_0 \cdot \gamma_{ij})}{(2\mu - \nu\theta/\sqrt{J_2'})} \times \left[1 - \exp\left[-\frac{\kappa(2\mu - \nu\theta/\sqrt{J_2'})t}{(\gamma_{ij}\gamma_{ij})^2}\right]\right] \qquad (21)$$

This solution is corresponded to Kelvin-Voigt rheology [9].

Return to eq. (16). For Kelvin-Voigt rheology the member $(\gamma_{ij}\gamma_{ij})^2 \cdot \kappa^{-1}$ is corresponded to viscosity, so that we'll call this member "effective viscosity" and denote η. So, we can finally write for effective viscosity of clay

$$(\gamma_{ij}\gamma_{ij})^2 \cdot \kappa^{-1} = \eta, \qquad (22)$$

and experimentally check the last correlation. For this purposes we use the simplest relation of Kelvin-Voigt rheological body

$$\varepsilon = (\sigma / E)\left[1 - \exp(-Et/\eta)\right]. \qquad (23)$$

Where E is the Young modulus. From equation (23) we can obtain the next relation for viscosity

$$\eta = \sigma / (d\varepsilon / dt)_{|t=0}. \qquad (24)$$

So, for experimental definition η in accordance with (24) we can use the classical compression experiment, carried out with a sample of clay of a specified mineral composition. At the time we'll measure the electro-conductivity of sample of the same clay, and after use the relation (22). Below we demonstrate results of measurements and its comparison with calculation's results.

On *Fig. 1* plots of measured values of electro-conductivity and viscosity of kaolinite are presented. Also calculated values of viscosity are shown.

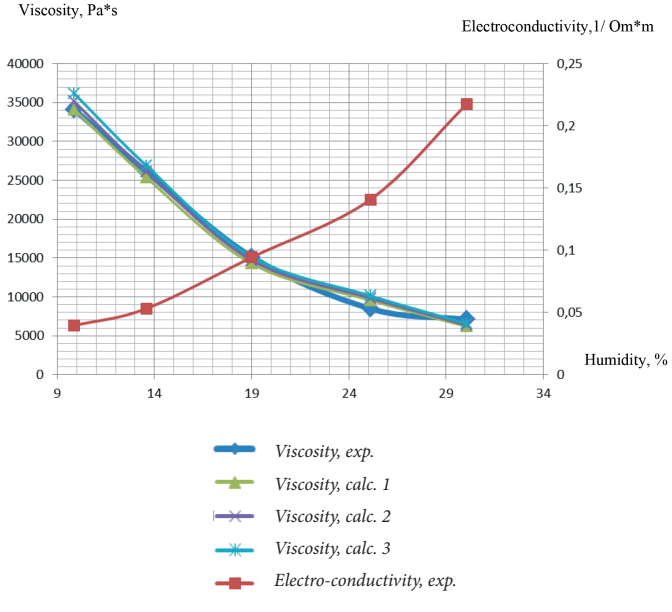

Fig. 1. The experimental (exp.) and calculated (calc.) values of viscosity and electro-conductivity of kaolinite in dependence on humidity. Definitions:
1. ábra Kísérleti és számított értékek kaolinit viszkozitására és elektromos vezetőképességére a nedvességtartalom függvényében.

One can see a good agreement between experimental and calculated data.

On *Fig. 2* plots of measured values of electro-conductivity and viscosity of mica are presented. Also calculated values of viscosity are shown. One also can see a good agreement between experimental and calculated data.

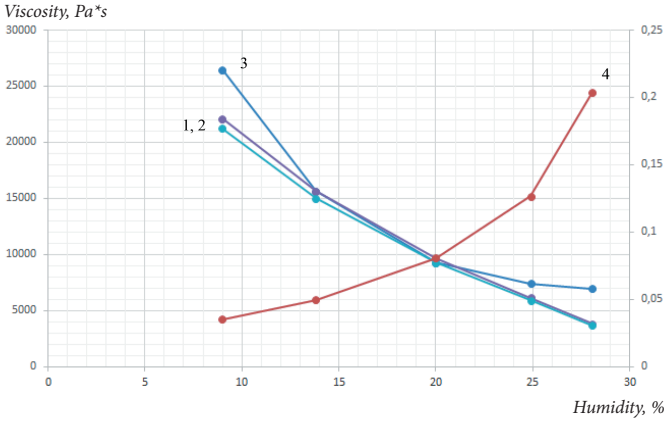

1, 2 – Viscosity, calc.
3 – Viscosity, exp.
4 – Electro-conductivity, exp.

Fig. 2. The experimental (exp.) and calculated (calc.) values of viscosity and electro-conductivity of mica in dependence on humidity. Definitions:
2. ábra Kísérleti és számított értékek csillám viszkozitására és elektromos vezetőképességére a nedvességtartalom függvényében.

In the case of montmorillonite clay we have to take into account additional impact to electro-conductivity of cations on basal surface of clay particles, and after we have to change the formula (22) for montmorillonite and obtain finally

$$\alpha(\gamma_{ij}\gamma_{ij})^2 \cdot \kappa^{-1,3} = \eta, \qquad (25)$$

where α is correction factor. On *Fig. 3* plots of measured values of electro-conductivity and viscosity of montmorillonite are presented. Also calculated values of viscosity are shown. One also can see a good agreement between experimental and calculated data.

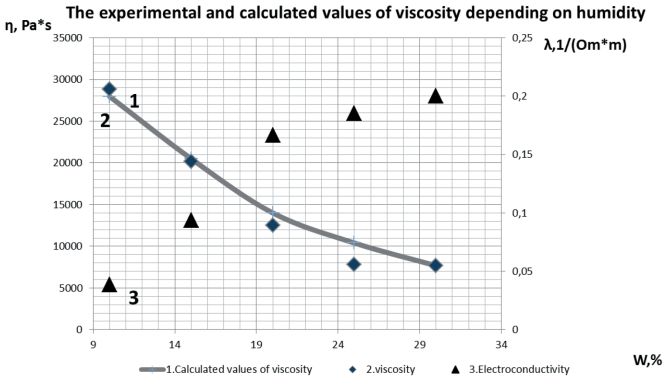

1 - Viscosity, calc.
2 - Viscosity, exp.
3 – Electro-conductivity, exp.

Fig. 3. The experimental (triangles and rhombuses) and calculated (line) values of viscosity and electro-conductivity of montmorillonite in dependence on humidity. Definitions:
3. ábra Kísérleti és számított értékek montmorillonit viszkozitására és elektromos vezetőképességére a nedvességtartalom függvényében.

4. Conclusions

It was important for us to offer a model of physical, electro-chemical and mechanical properties of clay, which doesn't use a priori any suppositions about the it's rheology, but use only known facts about properties of components of clayey rocks. Such a model was created by the unification of the theory of filtration consolidation and the theory of DLVO. On the base of this model we solved a simple problem of clay's rheological and electro-chemical properties and we showed that the model gives an ability to describe the rheology of clays with correlation of electro-chemical properties of clays, which was received experimentally. On the foundation of developing ideas we created the mathematical model of electro-chemical phenomena in clay. The correlations we've received are well co-ordinated with experiments. It's also showed that the developing is a physical substantiation of well-known hydrogeological schemes for calculation of yield clay water into the aquifer [10–11].

5. Acknowledgements

Authors thank RSCF, grant no. 15-11-10015.

References

[1] Mitchell, J. K.: Fundamentals of Soil Behavior. *John Wiley & Sons*, Inc. New York. 1976.

[2] Khramchenkov M. G. (2005): Rheological double-porosity model for clayey rocks. *International Journal of Rock Mechanics and Mining Sciences*, Vol. 42, pp 1006-1014. https://doi.org/10.1016/j.ijrmms.2005.05.013

[3] Khramchenkov M. – Khramchenkov E. (2014): A new approach to obtain rheological relations for saturated porous media. *International Journal of Rock Mechanics and Mining Sciences*, Vol. 72, pp. 49-53. https://doi.org/10.1016/j.ijrmms.2014.07.018

[4] Coussy O. (2000): Poromechanics. *Wiley, John & Sons*, London

[5] Fjaer E. – Holt R. M. – Hoursrud P. – Raaen A. M. – Risnes R. (2008): Petroleum Related Rock Mechanics. 2nd ed. Elsevier, Amsterdam and Oxford

[6] Jaeger J. C. – Zimmerman R. W. (207): Fundamentals of Rock Mechanics, 4th ed. Wiley, Oxford

[7] Charlez Ph. F. (1991): Rock Mechanics. *Editions Technip*, Paris

[8] Lyakhovskii V. A. – Myasnikov V. P. (1984): Fiz. Zemli. 1984, no. 10, pp. 71 – 75.

[9] Nikolaevskiy N. V. (1996): Geomechanics and fluid dynamics. *Kluwer Academic Publishers*, Dordrecht

[10] Schechter R. S. (1992): Oil Well Stimulation. *Prentice Hall*. New Jersey

[11] Economides M. – Nolte K. (2000): Reservoir Stimulation. Wiley

Ref.:
Khramchenkov, Maxim G. – **Usmanov,** Rustem M.: *Modeling of rheological and electro-chemical properties of hydrated clays*
Építőanyag – Journal of Silicate Based and Composite Materials, Vol. 69, No. 3 (2017), 110–113. p.
https://doi.org/10.14382/epitoanyag-jsbcm.2017.19

From Nuclear to Cogeneration – How a natural disaster can change the policy of a country

Abderrahmane MELLAK ▪ Director of Research Laboratory (LGPH), Hydrocarbons and Chemicals Faculty ▪ Mellakabder@yahoo.fr

Érkezett: 2017. 10. 19. ▪ Received: 19. 10. 2017. ▪ https://doi.org/10.14382/epitoanyag-jsbcm.2017.20

Abstract

One of the main lines of research that the author of present paper was particularly interested in [1] at the World Gas Conference in Paris, WGC2015, is the development of a new fuel for the Model Cell Systems in Japan. After the great Fukushima earthquake in 2011, when many nuclear power plants were shut down, alternative sources of alternative energy had to be found to meet the high demands of the industry and the Japanese population.

In this research and publication work, we believe that through scientific research and technological innovation, we can demonstrate the great ability to understand and solve major development problems, stimulate economic growth and towards the development of a country. In addition, the following points are discussed: Change in Japanese energy policy, the emergency measures taken and by what methods to achieve these objectives?

Keywords: energy, nuclear, cogeneration, energy policy, development

Kulcsszavak: energia, nukleáris, kapcsolt, energiapolitika, fejlődés

Prof. Abderrahmane MELLAK

Director of the Laboratory of Engineering Physics of Hydrocarbons and Professor and Researcher Lecturer at the Faculty of Hydrocarbons and Chemistry of the University of Boumerdes, Algeria. He is an engineer in Oil Drilling (graduated in Algeria) and also holds a DEA (Diploma of Advanced Studies), a DESS (Diploma of Specialized Higher Studies) and a PhD, obtained in French Universities. Responsible for a team of researchers, Head of Bachelor and Master Drilling Wells, frames of United Engineers, Master, the Magister and Doctorates. Member of the National Commission of University Habilitation Programs (CNH) and the National Commission for the Evaluation of Algerian Universities (CNE), the Ministry of Higher Education and Scientific Research. Participated in world congresses and national and international conferences with papers and has several publications in recognized national and international journals. Participated in several television round tables (Canal Algeria, UFC) on the Quality of Higher Education, the University-Business Relationship). Attended the 26th World Gas Congress (WGC), held in Paris from June 1st to 5th, 2015.

1. Introduction

Fossil-fueled thermal power plants (gas, oil, coal) produce electricity, especially during periods of peak demand (for example, during periods of extreme cold). The combustion of these energies releases heat which is used to heat water and transform it into steam. This is pressurized to drive a turbine coupled to an alternator that produces electricity.

During this process, much of the heat is lost (up to 60%) when it could be used for other purposes. The installation of a cogeneration system in the installation makes it possible to recover this heat which was previously lost, thus limiting the overall losses.

2. Change in Japanese energy policy

After the great earthquake in Fukushima, eastern Japan, which officially caused 16,000 deaths and 2,500 disappeared, Japan changed its energy policy by shutting down all nuclear power plants until security was restored of its facilities.

At present, the share of fossil fuels (petroleum, liquefied natural gas and coal) in the Japanese energy mix has increased to 88%, compared to 62% before the earthquake [2]. The change in this energy mix has not been without consequence and has caused many adverse side effects for Japan.

On the one hand, there has been a negative environmental impact and, on the other hand, the decline in the economic situation. At the environmental level, CO_2 emissions increased by 14% due to increased energy consumption of fossil fuels and from an economic point of view, the trade balance became negative because Japan had to import an enormous amount of fuel to meet its energy deficit [2].

3. Emergency measures taken

In this context, Japanese policy makers have defined energy policy by:

- The need to increase renewable energy [3];
- The creation of the Japanese hydrogen company;
- The Japanese government has set a very ambitious target of installing 1.4 million fuel cells by 2020 and 5.3 million fuel cells by 2030 (two cumulative targets). The fuel cell is a cogeneration technology (see *Fig. 1*) that produces electricity and heat by chemical means, there is a reaction to energy consumption. It contributes to the primary energy saving by its high efficiency.

Generally, in the power of the conventional system, only 40% of the primary energy can be used because about 60% will be lost as heat to the power plant or through losses during power transmission.

On the other hand, fuel cells allow about 95% of energy use with local heat and power. The result is a reduction of 1.3 tons of CO_2 emissions and a reduction in operating costs per year (a comparative example of consumption for a house in the Tokyo area using a gas boiler).

4. Which methods to achieve these objectives?

The list of challenges facing Japan in the coming years focuses on:

- Continued cost reduction through technical innovation and mass production: A new (4th generation) fuel cell model was updated;
- Improved performance of key devices (battery, fuel processor): The total cost has decreased through improved installation, commissioning and

transportation. For example, installation has become easier by reducing the total weight of the system. The commissioning time is also reduced by 40%.

- Reduction of the number of components by simplifying the whole system: The number of components has been reduced by 15%, and also the weight of the whole system is reduced by 15% (from 90 kg to 77 kg);
- The increase in the use of standard components: There is a 20% reduction in the platinum-metal alloy used for the battery (the component used to generate electricity from hydrogen).
- The expansion of the customer base of urban areas through development.
- Of a specific model of apartments: lower prices for the end user compared to the previous model and a 50% reduction compared to the first model published in 2009).
- The advanced development towards the hydrogen society (development of fuel cell system for a pure hydrogen energy source).

5. What is cogeneration?

Cogeneration (or co-generation: co = whole and generation = production) is the simultaneous production of two different forms of energy in the same power station.

The principle of cogeneration consists in producing mechanical energy (converted into electricity) and heat at the same time and in the same installation (an installation for several applications) and from the same source of energy. In the case where the heat is also re-used to produce cold, the term "tri-generation" is used.

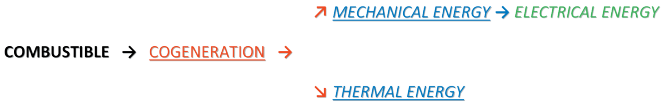

Fig. 1. Diagram of cogeneration
1. ábra Kapcsolt energiatermelés sémája

An engine (external or internal combustion), a turbine or a fuel cell is activated to produce electricity through some of the heat produced (the fuel may be natural gas, wood, fuel oil, biogas etc.). The remaining heat is used directly to heat water or produce steam.

In addition to reducing costs, the Japanese increased the product's durability to 70,000 hours and adopted DC power generation in the device [2].

In addition, it was launched a new model with the product heater for the outdoor market. Based on the large difference in demand for heat and cost between electricity and gas prices, one dares to believe that it has a strong potential market in European countries.

6. Problem statement

The serious problem facing Japan is the difference in the composition of the gas and the use of the fuel cell used in Japan and Europe:

- In Japan, gases are imported from abroad and purified during the liquefaction process. On the other hand, European countries import gas from pipelines from several sources. This results in instability in the fluctuation of the gas composition with a higher level of impurities in the gases compared to the LNG.
- In Japan, fuel cells are installed outside of each house and the demand for heat comes mainly from the hot water used for the bath, whereas in Europe, fuel cells are located inside the house (mainly in rooms and/or kitchens), which requires more air exhaust system (safety controls) and the heat is mainly intended for the heating of the spaces of the house. Research is underway in this area.

7. Conclusions

It can be concluded that the fuel cell is considered the key technology for smart homes. The introduction of cell fuel, in most homes and moving towards the concept of a city with a friendly environment and a pleasant and safe city with a goal of reducing CO_2 emissions by 70% compared to level of two decades ago.

Another application of cogeneration, which could become global is the incineration of large quantities, always increasing, of household waste. The burned waste produces heat. By installing a cogeneration system, this heat is recovered to produce water vapor that drives a turbine to produce electricity. This electricity can be consumed by the incineration plant or transferred to the electricity grid.

Also, the current trend in the field of research and innovation of technology goes towards the realization of a carbon-free hydrogen society at a reasonable cost and also move towards the evolution and expansion of the system fuel cells with high efficiency. Fuel cell is the basic technology for building the hydrogen society of the future in order to contribute to a better life and in part can contribute to the solution of environmental and climate cooperation and in harmony with various global partners.

References

[1] Mellak, Abderrahmane (2015), Professor of Universities, Director of Research Laboratory and Delegate of the AIG (Algerian Gas Association) at WGC2015 in Paris.

[2] M. Shimusu Toshiki (2015): Evolution of Residential Fuel Cell, *The Evolution of Ene-Farm at WGC2015 in Paris.*

[3] Mellak, Abderrahmane (2017): What Energy for Tomorrow? *? in International Science and Technology Conference (ISTEC 2017 America)*, Location: Harvard University Campus, Cambridge, MA, USA.

Ref.:
Mellak, Abderrahmane: *From Nuclear to Cogeneration – How a natural disaster can change the policy of a country*
Építőanyag – Journal of Silicate Based and Composite Materials, Vol. 69, No. 3 (2017), 114–115. p.
https://doi.org/10.14382/epitoanyag-jsbcm.2017.20

Assessment of reinforcement in polymer nanocomposites using cumulative rheological parameters

Milan KRACALIK ▪ Institute of Polymer Science, Johannes Kepler University ▪ Milan.Kracalik@jku.at

Érkezett: 2017. 10. 26. ▪ Received: 26. 10. 2017. ▪ https://doi.org/10.14382/epitoanyag-jsbcm.2017.21

Abstract

Multiphase polymer systems, like polymer nanocomposites, exhibit complex rheological behaviour due to physical and also possibly chemical interactions between individual phases. Up to now, rheology of dispersive polymer systems has been usually described by evaluation of viscosity curve (shear thinning phenomenon), storage modulus curve (formation of secondary plateau) or plotting information about dumping behaviour (e.g. Van Gurp-Palmen-plot, comparison of loss factor tan δ). On the contrary to evaluation of damping behaviour, values of cot δ were calculated and called as „storage factor", analogically to loss factor. Then values of storage factor were integrated over specific frequency range and called as "cumulative storage factor". In this contribution, LDPE-ZnO-clay nanocomposites with different dispersion grades (physical networks) have been prepared and characterized by both conventional as well as novel analysis approach. Next to cumulative storage factor, further cumulative rheological parameters like cumulative complex viscosity, cumulative complex modulus or cumulative storage modulus have been introduced.

Keywords: shear flow, oscillatory shear, polymer, clay, nanocomposites
Kulcsszavak: nyírási folyás, oszcilláló nyírás, polimer, agyag, nanokompozit

Prof. Dr. Milan KRACALIK
is assistant professor at the Institute of Polymer Science, Johannes Kepler University Linz. His field of expertise covers in particular polymer rheology, polymer composites and nanocomposites, polymer recycling, study of structure-properties relationship in polymer materials and management associated with technological processes and products. He studied Technology & Management at the Brno University of Technology, Czech Republic (MSc.: 2000), at Tomas Bata University in Zlin and Institute of Macromolecular Chemistry, Academy of Sciences of the Czech Republic (Ph.D.: 2006) associated with praxis in marketing department of Podravka-Lagris Inc., Czech Republic. Between 2006 and 2012 he was post-doc researcher & project leader at the Department of Polymer Engineering and Science of the University of Leoben, Austria. Between 2012 and 2014 he was research manager at the Department Research and Development of the ISOVOLTAIC AG, Austria. He has also lectured on Technology & Management at several European universities such as Albert Ludwigs University Freiburg, Budapest University of Technology and Economics, Chemical Research Centre / Hungarian Academy of Sciences, University of Zagreb and Department of Technical Sciences / Croatian Academy of Sciences and Art.

1. Introduction

Polymer nanocomposites using organically modified clays have been intensively investigated due to enhancement of processing as well as utility properties. Using nanoparticles is an interesting way for preparation of polymer tailored materials. The enhancement of material properties because of nanoparticles addition has usually been analysed using a combination of morphological (X-ray diffraction (XRD), transmission electron microscopy (TEM)), mechanical (tensile testing) and possibly rheological (rotational rheometry) measurements [1-17]. Using 2-5% of clay, significant improvement of material properties can be reached: high elastic modulus, tensile strength, thermal resistivity, low gas and liquid permeability, reduced flammability [18] and improved rheological properties compared to the unfilled polymer matrix [1-17]. High reinforcement due to addition of the layered silicates results from their large surface area (specific surface of montmorillonite is about 700-800 m^2/g) [19, 20]. In the case of highly dispersed systems, a three dimensional physical network is achieved, formed due to interactions between silicate platelets and the polymer chains. This phenomenon can be investigated by analysis of the melt elasticity using rotational rheometry [1-40]. These studies are mainly based on evaluation of viscosity curve shape (shear thinning phenomenon), storage modulus curve at low frequencies (formation of secondary plateau), phase homogeneity (Cole-Cole plot) or plotting information about dumping behaviour (e.g. Van Gurp-Palmen-plot, comparison of loss factor tan δ). In order to enable simple comparison of nanocomposites reinforcement in the shear flow, new way to analyze data of the shear flow has been tested [31, 32]. The storage modulus G´ describes the elastic part while the loss modulus provides us with information about the viscous part of the shear flow. The relation G´´/G´ is defined as tan δ and reflects damping behaviour in the polymer system. According available literature, the G´/G´´ ratio (cot δ) has not been used for rheological evaluation of nanocomposites up to now. Compared to tan δ (loss factor), cot δ (called as storage factor, SF) reflects melt rigidity, which can be associated with reinforcement effect in polymer (combination of chain elasticity with silicate layers rigidity in the polymer melt). In order to reduce the magnitudes of storage factor to one representative value for one sample, G´ as well as G´´ curves have been integrated over the measured frequency range as following:

$$CSF = \int_{0.1rad/s}^{628rad/s} G' \Big/ \int_{0.1rad/s}^{628rad/s} G'' \qquad (1)$$

In this way, cumulative storage factor (CSF) and some further cumulative rheological parameters (e.g. cumulative complex viscosity CCV, cumulative complex modulus CCM, cumulative storage modulus CSM) were introduced [31]. It was proven that values of CSF can be correlated with values of melt strength, i.e. the reinforcement in polymer nanocomposites can be assessed and compared in both, shear as well in elongational flow [32]. In this paper, LDPE-ZnO-clay nanocomposites with different dispersion grades (physical networks) are reported. It is shown that nano-scaled ZnO can be used not only as UV stabilizer but also as reinforcement and dispersion agent, respectively. The obtained data is analysed in this paper using typical rheological approaches as well as cumulative rheological parameters like CSF or CCV.

2. Materials and Method

CA9150 low-density polyethylene for extrusion coating has been used for the preparation of nanocomposites (supplied by Borealis Inc., Linz, Austria). The used nanoclay Cloisite 20 (Cl20) as well as LDPE masterbatch with 30% nano-scaled ZnO (Nanobyk) were supplied by BYK-Chemie Ltd, Wesel, Germany / POLYchem Ltd, Markt Allhau, Austria, respectively.

Mixtures have been prepared using laboratory compounder MiniLab II Haake Rheomex CTW5 (Thermo Fisher Scientific, Germany). Performance of four different compositions (pure PE matrix, 5wt.% of Cl20, 5wt.% of ZnO, 2.5/2.5 wt.% of Cl20/ZnO) have been compared. Rheological properties in the shear flow were studied using a Physica MCR 502 rheometer (Anton Paar Ltd., Graz, Austria) with the cone-plate geometry of 25 mm diameter and measuring gap of 43 μm.

3. Results & Discussion

The nanocomposites dispersion grade and effect of matrix molecular weight on final morphology can be evaluated using analysis of viscosity curve (shear-thinning effect) in combination with information obtained from the storage modulus curve (G´ secondary plateau; [33]). In *Figs. 1* and *2*, magnitudes of complex viscosity as well as storage modulus in dependency on angular frequency were plotted. As can be seen from *Fig. 1*, the systems prepared with Cl20 and Cl20/ZnO revealed pronounced shear-thinning behavior, as result of disruption of network structures and, consequently, by orientation of filler particles in flow. On the other hand, CA9150 matrix as well as nanocomposite only with ZnO showed typical liquid viscoelastic behaviour. The lower viscosity values of nanocomposite only with ZnO comparing with pure CA9150 matrix can be explained by significantly lower viscosity of LDPE matrix used for preparation of ZnO masterbatch. Therefore, higher admixture of ZnO masterbatch to CA9150 matrix results to higher "dilution" of CA9150 matrix, i.e. the average molecular weight in such polymer blend will be lowered.

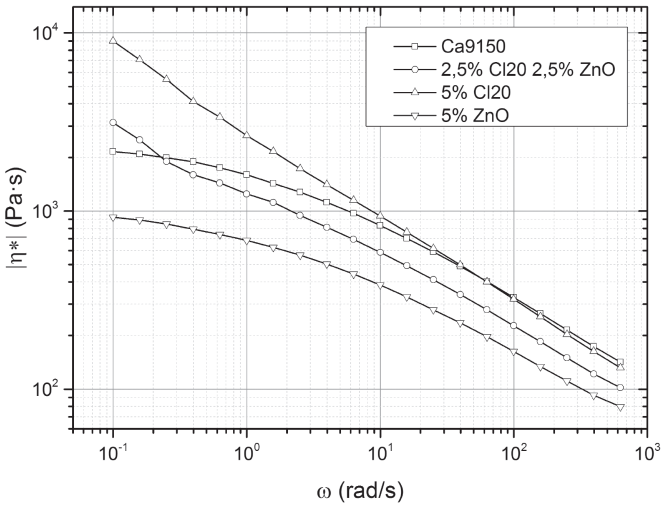

Fig. 1. Complex viscosity of nanocomposites
1. ábra Nanokompozitok komplex viszkozitása

For systems with high dispersion grade, the dependence of G´(ω) becomes almost invariable at low frequencies. Such "secondary" plateau indicates the formation of a network structure ("rubber-like" behavior) reflecting the exfoliation of silicate layers in nanocomposites [34, 47, 48]. As can be seen in *Fig. 2*, systems prepared with Cl20 and Cl20/ZnO showed "rubber-like" behaviour i.e. high dispersion grade, while pure CA9150 matrix as well as nanocomposite with ZnO exhibited typical viscoelastic behaviour. It means, in 2.5 Cl20/2.5 ZnO nanocomposite, two physical interactions are acting simultaneously: on one hand, melt elasticity is increased by formation of 3D-physical nework between polymer chains and silicate platelets, and, on the other hand melt elasticity is decreased due to decrease in polymer average molecular weight. As can be seen from *Figs. 1* and *2*, the decrease in polymer average molecular weight is dominating in 5% ZnO nanocomposite system comparing to pure CA9150 matrix.

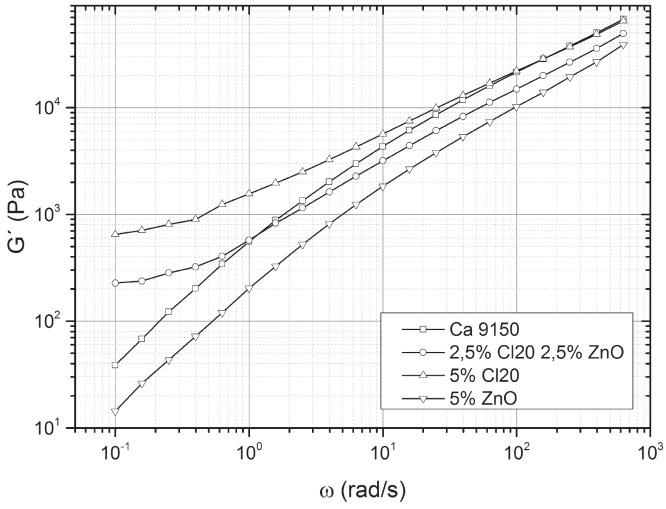

Fig. 2. Storage modulus of nanocomposites
2. ábra Nanokompozitok tárolási modulusa

The van Gurp-Palmen (vGP) plot as a dependency of loss angle δ on complex modulus |G*| can be used to analyze the spatial structures of polymers [41-45]. In *Fig. 3*, vGP plot is shown for prepared samples. For the polymer samples with rather linear chain structure, a continuous shaped curve has been published. On the contrary, long chain branched (LCB) polymers showed a developed bump between the |G*| minimum and the 90° plateau [44]. As can be seen in *Fig. 3*, systems prepared with Cl20 and Cl20/ZnO show spatial structure similar to mentioned LCB polymers with even two bumps or peaks (Cl20), indicating complex 3D structure made of filler and polymer chains [49]. The CA9150 matrix and nanocomposite with ZnO exhibit behaviour connected with linear chain structure. In order to get additional information about viscoelastic damping behaviour of the prepared samples, phase shift δ in dependency on angular frequency has been plotted (*Fig. 4*). The curves are similar to those of vGP and confirm formation of differently organized structures (combination of agglomerated, delaminated and exfoliated structure) depending on achieved 3D network.

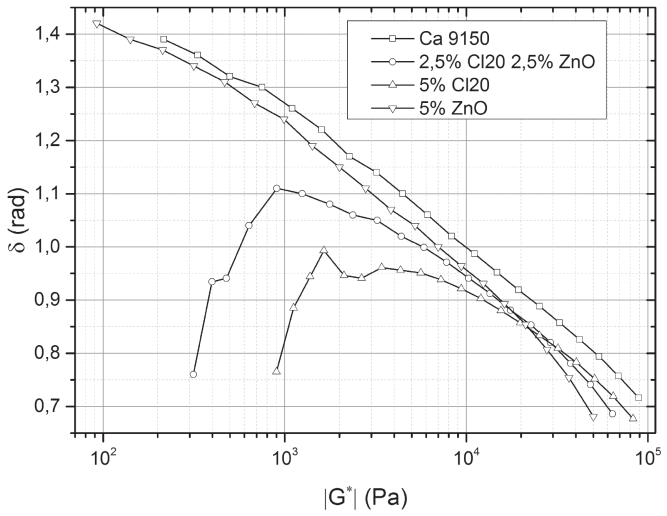

Fig. 3. Van Gurp-Palmen plot of nanocomposites
3. ábra Nanokompozitok Van Gurp-Palmen diagramja

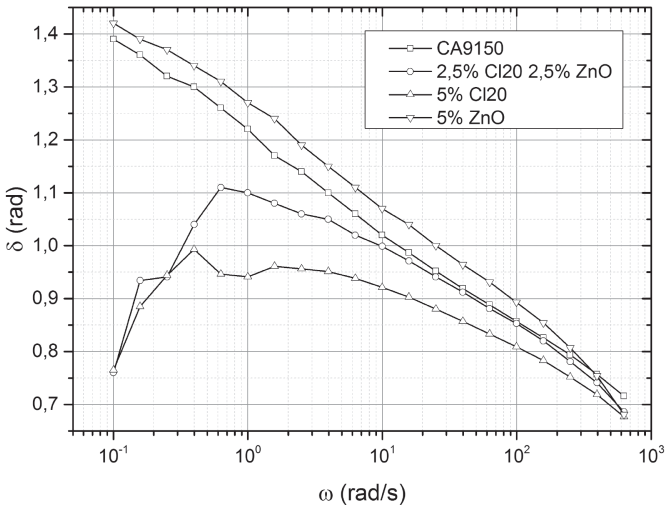

Fig. 4. Phase shift in dependency on angular frequency
4. ábra Fáziseltolódás a szögfrekvencia függvényében

Another approach for description of viscoelastic damping behaviour is so called "Cole-Cole" figure, in which imaginary part of complex viscosity over the real part is plotted. This figure has been widely used to assess miscibility/homogeneity of polymer blends and composites in the way that a smooth, semi-circular shape can be interpreted by better compatibility and homogeneity, respectively [23,46]. As shown in *Fig. 5* the CA9150 matrix and nanocomposite with ZnO showed semi-circle shapes, reflecting high homogeneity of the system. However, for the analysis of polymer nanocomposites performance, not only homogeneity but also reinforcement should be addressed. Using Cole-Cole plot, it can be said, that systems prepared with Cl20 and Cl20/ZnO revealed deviation from semi-circle shape and, therefore, are rather not homogeneous. Nevertheless, no information about reinforcement level can be obtained from this figure and this problem is actually concomitant with each previously described rheological analysis based on damping behaviour.

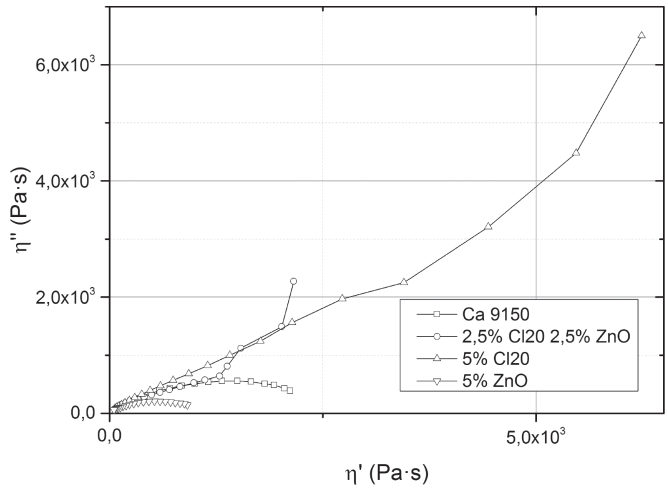

Fig. 5. Cole-Cole plot
5. ábra Cole-Cole diagram

Using previously introduced analysis based on "rigidity" behaviour [31, 32], there is possibility to analyze reinforcement level as result of 3D physical network between polymer chains and filler particles and, consequently, to obtain some information hidden in analysis based on damping behaviour.

The CSF plotted over CCV in *Fig. 6* shows clearly other trend as trends obtained from figures analyzed previously in this paper. For CA9150 matrix it can be seen that viscosity value is high, but reinforcement level represented by CSF (comparing to all nanocomposites) is low. Comparing to CA9150, the nanocomposite with 5% of ZnO revealed lower value of viscosity, but higher value of reinforcement, followed by nanocomposite with 2.5/2.5 wt.% of Cl20/ZnO and finally followed by nanocomposite with 5wt.% of Cl20 showing the highest reinforcement and approximately same level of viscosity. In this way, it was possible to divide contribution of "internal reinforcement" coming from internal friction (high molecular weight and viscosity values, respectively) – represented by viscosity values – and "external reinforcement" coming from 3D physical network between polymer chains and nanofiller particles – represented by CSF values. This division was not possible to analyze using evaluation methods based on damping behaviour.

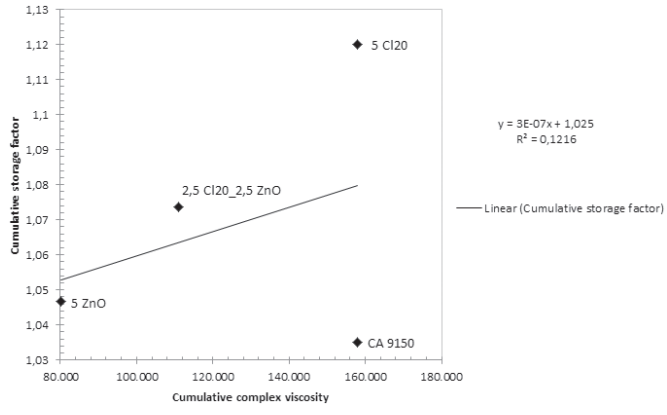

Fig. 6. Cumulative storage factor
6. ábra Kumulatív tárolási tényező

Comparing to *Fig. 6*, coefficient of linear regression in *Fig. 7* is very high. It means, if only polymer nanocomposites are compared, there is high correlation between CSF and CCV values, giving possibility to compare previously described "external reinforcement" not only in cases of nanocomposites using one polymer matrix, but also in cases of nanocomposites based on polymer blends. This result will be proved in further work using not only polymer matrices with different molecular weight but also with different chemical compositions.

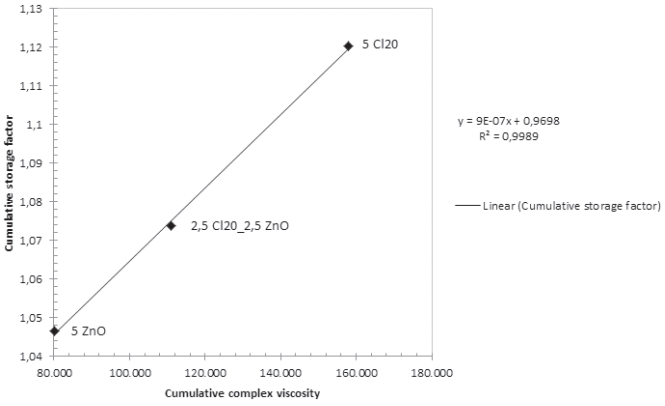

Fig. 7. Cumulative storage factor of nanocomposites without neat matrix
7. ábra Nanokompozitok kumulatív tárolási tényezője ágyazóanyag nélkül

4. Conclusions

Complex polymer nanocomposites with different molecular weight polyethylenes and clay/ZnO nanoparticles were prepared and analyzed by conventional as well by new rheological approach. Using novel approach based on melt rigidity analysis the reinforcement caused by 3D physical network between polymer chains and nanofiller particles could be divided from that coming from internal friction (polymer molecular weight). In this way, new inside into performance characterization of polymer nanocomposites has been introduced and will be tested on nanocomposites based on different polymer blends in future work.

References

[1] Ray S. S. – Okamoto M. (2003): Polymer/layered silicate nanocomposites: a review from preparation to processing. *Progress in Polymer Science*, 28:1539-1641. https://doi.org/10.1016/j.progpolymsci.2003.08.002

[2] Ray S. S. – Yamada K. – Okamoto M. – Ueda K. (2003): New polylactide-layered silicate nanocomposites. 2. *Concurrent improvements of material properties, biodegradability and melt rheology*. Polymer, 44:857-866. https://doi.org/10.1016/S0032-3861(02)00818-2

[3] Laske S. – Witschnigg A. – Mattausch H. – Kracalik M. – Pinter G. – Feuchter M. – Maier G. – Holzer C. (2012): Determining the ageing of polypropylene nanocomposites using rheological measurements. *Applied Rheology*, 22 (2), 24590 – 24599. https://doi.org/10.3933/ApplRheol-22-24590

[4] Abdel-Goad M. (2011): Rheological characterization of melt compounded polypropylene/clay nanocomposites. *Composites Part B*, 42: 1044–1047. https://doi.org/10.1016/j.compositesb.2011.03.025

[5] Aghjeh M. R. – Asadi V. – Mehdijabbar P. et al. (2015): Application of linear rheology in determination of nanoclay localization in PLA/EVA/Clay nanocomposites: Correlation with microstructure and thermal properties. *Composites Part B*, 86: 273–284. https://doi.org/10.1016/j.compositesb.2015.09.064

[6] Ahmed J. – Auras R. – Kijchavengkul T. et al. (2012): Rheological, thermal and structural behavior of pol (e-caprolactone) and nanoclay blended films. *Journal of Food Engineering*, 111: 580–589. https://doi.org/10.1016/j.jfoodeng.2012.03.014

[7] Filippone G. – Carroccio S. C. – Curcuruto G. et al. (2015): Time-resolved rheology as a tool to monitor the progress of polymer degradation in the melt state e Part II: Thermal and thermo-oxidative degradation of polyamide 11/organo-clay nanocomposites. *Polymer*, 73: 102–110. https://doi.org/10.1016/j.polymer.2015.07.042

[8] Mishra J. K. – Hwang K-J. – Ha C-S. (2005): Preparation, mechanical and rheological properties of a thermoplastic polyolefin (TPO)/organoclay nanocomposite with reference to the effect of maleic anhydride modified polypropylene as a compatibilizer. *Polymer*, 46: 1995–2002. https://doi.org/10.1016/j.polymer.2004.12.044

[9] Nobile M. R. – Simon G. P. – Valentino O. et al. (2007): Rheological and Structure Investigation of Melt Mixed Multi-Walled Carbon Nanotube/PE Composites. *Macromolecular Symposia 247: 78–87*. https://doi.org/10.1002/masy.200750110

[10] Sadeghipour H. – Ebadi-Dehaghani H. – Ashouri D. et al. (2013): Effects of modified and non-modified clay on the rheological of high density polyethylene. *Composites: Part B*, 52: 164–171. https://doi.org/10.1016/j.compositesb.2013.04.010

[11] Samyn F. – Bourbigot S. – Jama C. et al. (2008): Crossed characterisation of polymer-layered silicate (PLS) nanocomposite morphology: TEM, X-ray diffraction, rheology and solid-state nuclear magnetic resonance measurements. *European Polymer Journal 44*: 1642–1653. https://doi.org/10.1016/j.eurpolymj.2008.03.021

[12] Wagener R. – Reisinger T. J. G. (2003): A rheological method to compare the degree of exfoliation of nanocomposites. *Polymer*, 2003(44): 7513–7518. https://doi.org/10.1016/j.polymer.2003.01.001

[13] Wang M. – Fan X. – Thitsartarn W. et al. (2014): Rheological and mechanical properties of epoxy/clay nanocomposites with enhanced tensile and fracture toughnesses. *Polymer*, 58: 43–52. https://doi.org/10.1016/j.polymer.2014.12.042

[14] Zhang X. – Yang G. – Lin J. (2006): Synthesis, Rheology, and Morphology of Nylon-11/Layered Silicate Nanocomposite. Journal of Polymer Science: Part B: *Polymer Physics*, 44: 2161–2172. https://doi.org/10.1002/polb.20881

[15] Zhao J. – Morgan A. B. – Harris J. D. (2005): Rheological characterization of polystyrene-clay nanocomposites to compare the degree of exfoliation and dispersion. *Polymer*, 2005(46): 8641–8660. https://doi.org/10.1016/j.polymer.2005.04.038

[16] Zhao Y. – Huang H-X. (2008): Dynamic rheology and microstructure of polypropylene/clay nanocomposites prepared under Sc-CO_2 by melt compounding. *Polymer Testing*, 27: 129–134. https://doi.org/10.1016/j.polymertesting.2007.11.006

[17. Zhong Y. – Zhu Z. – Wang S-Q. (2005): Synthesis and rheological properties of polystyrene/layered silicate nanocomposite. *Polymer*, 46 (3006-3013). https://doi.org/10.1016/j.polymer.2005.02.014

[18] Gilman J. – Kashiwagi T. – Lichtenhan J. (1997): Nanocomposites: A revolutionary new flame retardant approach. *Sampe Journal*, 33:40–46.

[19] Lee K. M., Han C. D. (2003): Rheology of Organoclay Nanocomposites: Effects of Polymer Matrix/Organoclay Compatibility and the Gallery Distance of Organoclay. *Macromolecules*, 36:7165-7178. https://doi.org/10.1021/ma030302w

[20] Lee K. M. – Han C. D. (2003): Effect of hydrogen bonding on the rheology of polycarbonate/organoclay nanocomposites. *Polymer*, 44:4573-4588. https://doi.org/10.1016/S0032-3861(03)00444-0

[21] Ahmed J. – Varhney S. K. – Auras R. – Hwang S. W. (2010): Thermal and rheological properties of L-polylactide/polyethylene glycol/silicate nanocomposites films. *Journal of Food Science*, 75: N97–N108. https://doi.org/10.1111/j.1750-3841.2010.01809.x

[22] Ahmed J. – Auras R. – Kijchavengkul T. – Varshney S. K. (2012): Rheological, thermal and structural behavior of poly(e-caprolactone) and nanoclay blended films. *Journal of Food Engineering*, 111: 580–589. https://doi.org/10.1016/j.jfoodeng.2012.03.014

[23] Aklonis J. J. – Macknight W. J. (1983): Introduction to viscoelasticity. *New York: Wiley*; 1983.

[24] Gelfer M. – Song H. H. – Liu L. – Avila-Orta C. – Yang L. – Si M. – Hsiao B. S. – Chu B. – Rafailovich M. – Tsou A. H. (2002): Manipulating the microstructure and rheology in polymer-organoclay composites. *Polymer Engineering and Science*, 42:1841-1851. https://doi.org/10.1002/pen.11077

[25] Hoffmann B. – Dietrich C. – Thomann R. – Friedrich C. – Mülhaupt R. (2000): Morphology and rheology of polystyrene nanocomposites based upon organoclay. *Macromolecular Rapid Communications*, 21:57-61. https://doi.org/10.1002/(SICI)1521-3927(20000101)21:1<57::AID-MARC57>3.0.CO;2-E

[26] Hoffmann B. – Kressler J. – Stöppelmann G. – Friedrich C. – Kim G. M. (2000): Rheology of nanocomposites based on layered silicates and polyamide-12. *Colloid and Polymer Science*, 278:629-636. https://doi.org/10.1007/s003960000294

[27] Hyun Y. H. – Lim S. T. – Choi H. J. – Jhon M. S. (2001): Rheology of Poly(ethylene oxide)/Organoclay Nanocomposites. *Macromolecules,* 34:8084-8093. https://doi.org/10.1021/ma002191w

[28] Incarnato L. – Scarfato P. – Scatteia L. – Acierno D. (2004): Rheological behavior of new melt compounded copolyamide nanocomposites. *Polymer*, 45:3487-3496. https://doi.org/10.1016/j.polymer.2004.03.005

[29] Kim T. H. – Jang L. W. – Lee D. C. – Choi H. J. – Jhon M. W. (2002): Synthesis and Rheology of Intercalated Polystyrene/Na+-Montmorillonite Nanocomposites. *Macromolecular Rapid Communications*, 23:191-195. https://doi.org/10.1002/1521-3927(20020201)23:3<191::AID-MARC191>3.0.CO;2-H

[30] Kotsilkova R. (2002): Rheology–Structure Relationship of Polymer/Layered Silicate Hybrids. *Mechanics of Time-Dependent Materials*, 6:283-300. https://doi.org/10.1023/A:1016226118991

[31] Kracalik M. (2015): Rheology of Multiphase Polymer Systems using Novel „Melt Rigidity" Evaluation Approach. *AIP Conference Proceedings*, 1662: 040002-1 – 040002-6. https://doi.org/10.1063/1.4918890

[32] Kracalik M. – Laske S. – Witschnigg A. – Holzer C. (2011): Elongational and shear flow in polymer-clay nanocomposites measured by on-line extensional and off-line shear rheometry. *Rheologica Acta*, 50 (11-12): 937-944. https://doi.org/10.1007/s00397-011-0545-2

[33] Kracalik M. – Mikesova J. – Puffr R. – Baldrian J. – Thomann R. – Friedrich C. (2007): Effect of 3D Structures on Recycled PET/Organoclay Nanocomposites. *Polymer Bulletin*, 58:313-319. https://doi.org/10.1007/s00289-006-0592-5

[34] Krishnamoorti R. – Giannelis E. P. (1997): Rheology of End-Tethered Polymer Layered Silicate Nanocomposites. *Macromolecules*, 30:4097-4102. https://doi.org/10.1021/ma960550a

[35] Mohagheghian M. – Ebadi-Dehaghani H. – Ashouri D. – Mousavian S. (2011): A Study on the effect of nano-ZnO on rheological and dynamic mechanical properties of polypropylene: experiments and models. *Composites: Part B*, 42:1987–93. https://doi.org/10.1016/j.compositesb.2011.04.043

[36] Sadeghipour H. – Ebadi-Dehaghani H. – Ashouri D. – Mousavian S. – Hashemi-Fesharaki M. – Gahrouei M. S. (2013): Effects of modified and non-modified clay on the rheological behaviour of high density polyethylene. *Composites: Part B*, 52: 164–171. https://doi.org/10.1016/j.compositesb.2013.04.010

[37] Sanchez-Solis A. – Garcia-Rejon A. – Manero O. (2003): Production of nanocomposites of PET-montmorillonite clay by an extrusion process. *Macromolecular Symposia*, 192:281-292. https://doi.org/10.1002/masy.200390038

[38] Sanchez-Solis A. – Romero-Ibarra I. – Estrada M. R. – Calderas F. – Manero O. (2004): Mechanical and rheological studies on polyethylene terephthalate-montmorillonite nanocomposites. *Polymer Engineering and Science*, 44:1094-1102. https://doi.org/10.1002/pen.20102

[39] Solomon M. J. – Almusallam A. S. – Seefeldt K. F. – Somwangthanaroj A. – Varadan P. (2001): Rheology of Polypropylene/Clay Hybrid Materials. *Macromolecules*, 34:1864-1872. https://doi.org/10.1021/ma001122e

[40] Wagener R. – Reisinger T. J. G. (2003): A rheological method to compare the degree of exfoliation of nanocomposites. *Polymer*, 44:7513-7518. https://doi.org/10.1016/j.polymer.2003.01.001

[41] Lohse D. J. – Milner S. T. – Fetters L. J. – Xenidou M. – Hadjichristidis N. – Mendelson R. A. – Garcia-Franco C. A. – Lyon M. K. (2002): Well-defined, model long chain branched polyethylene. 2. melt rheological behaviour. *Macromolecules*, 35:3066-3075. https://doi.org/10.1021/ma0117559

[42] Schulze D. – Trinkle S. – Mulhaupt R. – Friedrich C. (2003): Rheological evidence of modifications of polypropylene by β-irradiation. *Rheologica Acta*, 42:251-258. https://doi.org/10.1007/s00397-002-0282-7

[43. Trinkle S. – Friedrich C. (2001): Van Gurp-Palmen plot: a way to characterize polydispersity of linear polymers. *Rheologica Acta*, 40:322-328. https://doi.org/10.1007/s003970000137

[44] Trinkle S. – Walter P. – Friedrich C. (2002): Van Gurp-Palmen plot II – classification of long chain branched polymers by their topology. *Rheologica Acta*, 41:103-113. https://doi.org/10.1007/s003970200010

[45] Van Gurp M. – Palmen J. (1998): Time-temperature superposition for polymeric blends. *Rheology Bulletin*, 67:5-8.

[46] Utracki L. A. (1999): Polymer blends handbook. *Netherlands: Kluwer Academic Publishers*

[47] Khan, S. A. – Pruđhomme, R. K. (1987): Melt Rheology of Filled Thermoplastics. *Reviews in Chemical Engineering*, 1987, 4, 205. https://doi.org/10.1515/REVCE.1987.4.3-4.205

[48] Krishnamoorti, R. – Vaia, R. A. – Giannelis, E. P. (1996): Structure and Dynamics of Polymer-Layered Silicate Nanocomposites. *Chemistry of Materials*, 1996, 8, 1728. https://doi.org/10.1021/cm960127g

[49] Chevallier C. – Becquart F. – Taha M. (2013): Polystyrene/polycarbonate blends compatibilization: Morphology, rheological and mechanical properties. *Materials Chemistry and Physics*, 139: 616–622. https://doi.org/10.1016/j.matchemphys.2013.02.006

Ref.:
Kracalik, Milan: *Assessment of reinforcement in polymer nanocomposites using cumulative rheological parameters*
Építőanyag – Journal of Silicate Based and Composite Materials, Vol. 69, No. 3 (2017), 116–120. p.
https://doi.org/10.14382/epitoanyag-jsbcm.2017.21

Biomechanical Evaluation of Lumbosacral Segments Response under Physiological Functions: Finite Element Analysis

Mohammed BENDOUKHA ▪ Laboratory of Numerical and Experimental Modeling of Mechanical Phenomena, Department of Mechanical Engineering, University Abd El Hamid IbnBadis ▪ bendoukham@yahoo.fr

Mustapha MOSBAH ▪ Laboratory of Numerical and Experimental Modeling of Mechanical Phenomena, Department of Mechanical Engineering, University Abd El Hamid IbnBadis

Érkezett: 2017. 10. 26. ▪ Received: 26. 10. 2017. ▪ https://doi.org/10.14382/epitoanyag-jsbcm.2017.22

Abstract

The basic key in the process of our validation may be stated in the development of computational analogues of the spinal morphologies by the creation of sophisticated 3-dimensional Finite Element (FE) model of an intact ligamentous L1–S1 motion segment that matches the real biomechanical behavior of the human lumbosacral spine and for this purpose, the curves were found to be non-linear and the Ranges of Motion (ROM) results were found to compare favorably with reported values from in vivo and in vitro studies as documented in experiments conducted on human cadavers [1, 2]. Therefore, this FE-model can be used to investigate the stress and strain distributions in the L1-S1components, especially the discs under physiological functions such as heavy and daily carrying tasks it has the possibility of representing the realities with a much higher degree of fidelity.

Keywords: Finite Element, lumbar spine behavior, ranges of motion, in vivo, in vitro

Kulcsszavak: végeselem, ágyéki gerinc viselkedése, mozgástartomány, in vivo, in vitro

Mohammed BENDOUKHA

Research Professor at the University of Mostaganem. Obtained his Engineering degree in Mechanical Engineering from the University of Science and Technology of Oran (USTO). After postgraduation studies he obtained Magister at the USTO IN 1991. Obtained his PhD in tribology speciality in 2010 at the University of Mostaganem, and subsequently his habilitation to direct the research of the same university in 2011. He is active in the field of research at the laboratory of numerical and experimental modeling of mechanical phenomena.

Mustapha MOSBAH

PhD candidate in biomechanics under the supervision of Dr. BENDOUKHA at the laboratory of numerical and experimental modeling of mechanical phenomena. Obtained the licence and Master's degree from the University of Mostaganem in Mechanics.

1. Introduction

The aim of this work is to make an accurate computational FE-model to simulate the biomechanical response of the human lumbar spine under physiological functions. Its success at simulation is not insured but must be tried out by suitable validation to insure the accuracy of any FE-model. The model is conceived as regards validated if, in circumscribed number of offices, its predicted behavior comes close to the experimental results. It is then assumed that the model may now be exercised to predict behavior of the structure in other situations by knowledge of regular spinal movements [3], The lumbar region is a recurring set of spinal disorders [4, 5]. Clinical studies have testified that abnormal intervertebral motions occur in some patients who have low-back pain and the utmost proportion (about 90%) of spinal disorders is located in the lumbar spine segment [6].

While, in the absence of pathological disease, regular daily activities, lifting stationary work postures, heavy physical work and vibrations are factors that contribute to low back disorders [7, 8]. Usually, orthopedic treatment is essentially based on the experience of the surgeon who predicts the best solution for each patient. Using mathematical models and computer simulations could hypothetically be a key tool that supports clinical decisions in order to predict the presence and evolution of spine pathologies, for preoperative planning and implant design. [9, 10, 11]. The present work is concentrates on the analysis of the lumbar spine with the objective of studying of the influence and the roles that the different components of the spine play on its biomechanical response, in particular the presence of an injury in the intervertebral disc (IVD).

In order to understand the whole lumbosacral segments response under physiological conditions, the complete three-dimensional elastic physical properties of the lumbar spine were precisely documented, then, (L1–S1) rachis FE-model was built and their mechanical responses under static loading were predicted. [11, 12].

Pure moments of flexion-extension, in lateral axial torque, and in lateral, lateral bending were applied, and three-dimensional intervertebral motions were determined. The motions were presented in the form of a set of six load-displacement curves, quantifying the intervertebral rotations and translations. The current model should preserve the anatomical details required to simulate the biomechanical response, including tissue material properties appropriate for treatment of spinal disorders, and be validated in relevant loading scenarios.

2. Methods and materials

The main procedure is employed hierarchical approaches to develop a biomedical validated computational model of the lumbar spine to investigate the spinal disorders and diseases [11, 13].

An Osseo-ligaments FE-model of the L1-S1 levels was built and validated through comparison with literature data. An extended description of the model and its adaptation for the present study are outlined below in this study. The developed lumbar spine FE-model was created based on anatomically accurate geometries and was modeled based on the epidemiology of injuries and disease due to the literature [1, 13, 11]. FE Analyses were performed using a 3-Dimensional

nonlinear model of the spine arraying from L1 to S1, created following multiple processes (*Fig. 2*).

The global geometry was derived from a CT scan based on the reconstitution of the L5/S1 FSU Data taken from a male cadaver what did not have any trauma or pathology that affect bone quality and integrity of vertebral bodies, then translated to patch iges model then to a simplified solid model using Power surfacing (Solid works 2013). (*Fig. 1*)

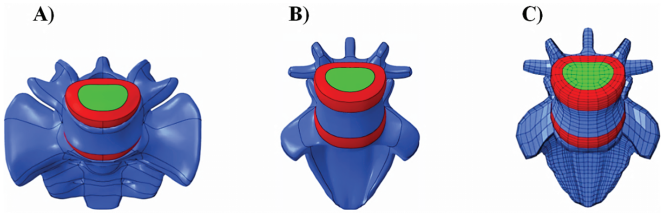

Fig. 1. A) Realistic L5/S1 Geometric Model, B) Simplified Power Surfacing Geometric Model, C) Generated Meshed Model using Ansys
1. ábra A) Realisztikus L5/S1 geometriai modell, B) egyszerűsített hatványfelület geometriai modell, C) Ansys szoftverrel generált modell hálója

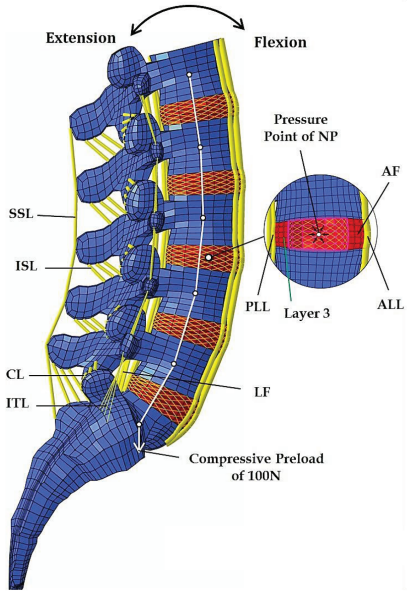

Fig. 2. Finite element model of the lumbosacral spine L1–S1 and intra discal pressure point
2. ábra Lumboszakrális L1–S1 gerinc szakasz végeselemes modellje és intradiszkális nyomáspont

This geometrical simplification allowed the full optimization of an accurate three dimensional model. The reconstructed Solid model of L5/S1 was derived from a commercial model of the spine (Zygote Media Group – American Fork, UT, USA). The geometry of the vertebra and the intervertebral disc was approximated to match the realistic model of normal cadaveric lumbar segments. The model of a Lumbar Spine was developed using ANSYS revision 15.0 (ANSYS Inc., Houston, PA, USA). However, fully automated hexahedral mesh generation is not available for complex geometric entities such as the human lumbar spine. Utilizing hexahedral elements to effectively model the complexly shaped lumbar spine is not trivial and requires a substantial amount of work to subdivide the geometry in preparation for mesh generation. This meshing is desirable for FE analysis due to the nature of their shape function and ability to handle large deformations without creating numerical instabilities.

Concerning the parametric meshing, the developed spinal mesh was symmetrically modeled across the midsagittal plane as adopted in the literature [15], the mesh density and geometry was defined to represent the key passive anatomical features: cortical and cancellous bone; endplates; posterior elements of the vertebrae; annulus fibrosis and nucleus pulposus; articular cartilage; synovial fluid of the facet joint [11, 12]. 8-noded solid element (C3D8) were used to define The cancellous bone and posterior elements of the vertebrae and articular cartilage of the facet joints ,the cortical bone and endplates of the vertebrae and elsewhere using hexahedral element based on hybrid formulation for hyperelastic structure for the Annulus Pulposus (AP). Cortical bone and endplates of the vertebrae modeled using 8-noded brick elements with 0.635 mm thickness. [14, 15] .The commercial FE package Abaqus, version 14.1 was used to formulate the FE-model.

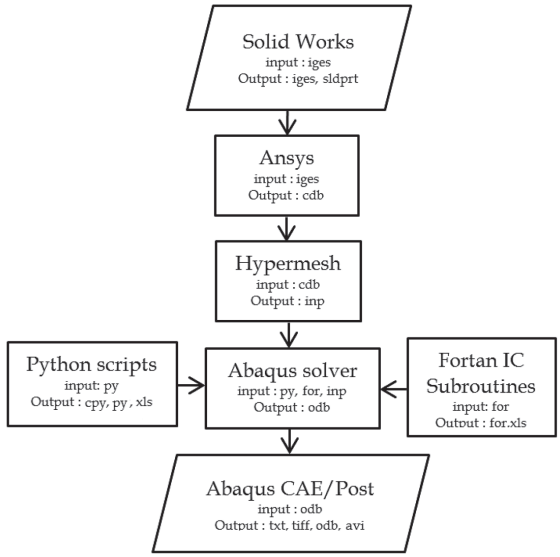

Fig. 3. Finite Element Model, Formulation Workflow Chart
3. ábra Végeselemes modell generálási folyamatábra

3. Numerical investigation

3.3 L1-S1 motion segment validation

3.3.1 Boundary and Loading Conditions

A well-defined Hybrid protocol was used to study the lumbosacral spine behavior. This key issue analysis reestablishes to principle applied load on the motion segments of pure momentum increasing incrementally from zero to 10 N.m (2.5, 5, 7.5, 10 N.m). Compressive follower preload of 100 N was applied in all modalities to the intact lumbar spine model in the follower load path direction, settled as suggested thereby allowing the axial load to follow the motion of the spine [9]. The Follower load was applied to the center of the vertebra through a Reference Node Constrained to the vertebral body nodes using Coupling Constraints Elements (CCE). The resulting FE-model was positioned in static Momentum Loads to match the experiment. Homogeneous Dirichlet boundary conditions were applied to all bottom side nodes, not involved

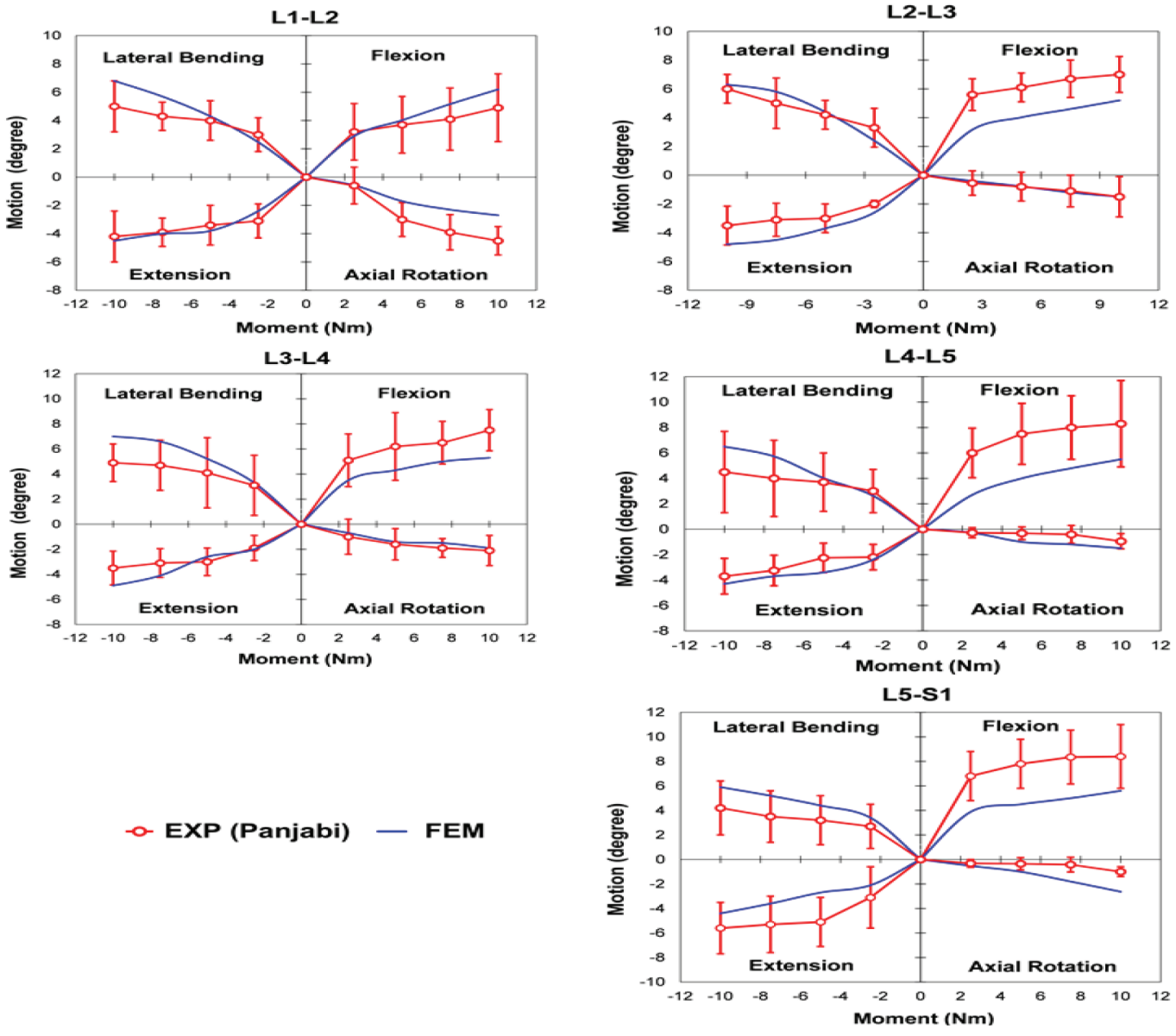

Fig. 4. Comparison between predicted intervertebral rotations results in different spinal levels for the loading cases flexion, extension, lateral bending, and axial rotation
4. ábra Porckorong elmozdulások összehasonlítása a gerinc különböző szintjein; hajlítás, megnyúlás, keresztirányú hajlítás, tengelyirányú elfordulás

in the motion procedure. The interpedicular displacement was predicted for the intact model in all directions, comparing with that of previous experimental studies [2]. Introduce the generated lumbar spine model not only allows personalized biomechanical analysis, but it also offers detailed geometric data to simplify simulation to mimic the realistic Lumbar spine. Knowledge of the normal motions of the whole lumbar spine and lumbosacral joint is important for evaluating clinical pathologic conditions.

3.3.3 Results

The results display a greater no-linearity of the spine response. Under load combination, the ROM of most of the dedicated FSU level, respectively from L1 to S1 is within the range of in vitro measurements as shown in *Fig. 4*, except a reduction of the predicted ROM in flexion, where the mobility is smaller than what is expected (L2-L3, L4-L5, L5-S1), taking into account in vitro conditions. In lateral bending and in axial rotation, the movement amplitudes are close to those found in the literature measurements as shown in *Fig. 4*. In particular, in extension, such as for the other movements, ROM are within the range of movements performed by the experimental ones especially for L1-L2, L2-L3, L3-L4 segments. Except for the segment L5-S which performs a little lower extension than in vitro measure, at L1-L2 level for extension in which we obtain a value of 4.2° against the experimental value of 4°. The numerical model in extension for the L4-L5 segment shows a deviation of 0.5° against the calculated experimental values.

The curves are similar with slightly higher rotation angles for the model in Axial Rotation for L4-L5 and L5/S1.

The segment L2-L3, L4-L5 shows the best results with an error of 0.1° and for the L3-L4 segment with a deviation of 0.2 between the FE-model and experimental. The maximum

flexion moment ROM of the segments L1-L2 is higher than for the other segments, the maximum rotation value has little variation between upper (-6.1° for L1-L2 level) and lower (-5.8° for L4-S1) segments. The FE-models are obtained at the L2-L3 level a deviation of 0.2° in the lateral bending and represent a deviation of 0.8° for the Axial Rotation of L5-S1.

4. Discussion

Validation of Any new finite element model should be observed the correlation between FE predictions and in vitro data to correctly reproduce key aspects of in vitro response of the lumbar spine. The Rotations-Displacement curves from the generated FE-model shows good accuracy of the experimental kinematics measurements. This FE-model of a human L1-S1 motion segment was used to explore the effect of daily physiological loads on the overall behavior of the lumbar spine. The ROM configuration of the model matches the experiment well for the overall L1-S1 endpoints. The loading applied to the model was formulated to simulate the observed physiological functions. The finite element modeling has long been used in biomechanical studies for research concerning clinical pathologies of the lumbar spine as well as for predicting the biomechanical characteristics. The lumbar spine model was developed to investigate the disc behavior and the whole L1-S1 functions under physiological conditions. The focus of this study was a validation of the theme shing, and FE-model generation procedure, with the latter step comprising construction and of the lumbar model L1-S1. This model generation step requires a substantial time commitment.

The geometric assumptions made in the development of the model were intended to allow an anatomically detailed representation of the Posterior-Anterior column. The computational results presented in this study represent an attempt to explore the role of passive spinal structures in generating rotations displacements accompanying primary spinal motions. We presented a finite element model for an isotropic with homogenous properties of the IVD, and the mechanical properties such as the non-linear behavior of the spinal ligaments. Healthy osseo ligamentous lumbosacral spine with all intact ligaments and a hydrostatic nucleus pulposus (1) The structure of the vertebral body was assumed as (2) The loading conditions were not truly physiological, because of the lack of the mechanical effects of muscular contraction forces which change with upper trunk position [3, 14].

5. Limitations of the FE analysis

As with all finite element model research, there are some inherent limitations of the models used: To realize a better resolution and results, it might be essential to refine the mesh which steer more anatomic details, require significant sensitivity analysis with more elements and nodes, including more degrees of freedom. These additions would have inconveniently increased the computation time and necessitate expense of computation power. The geometry of the IVD was based on realistic 3d model reconstituted from slice imaging scans but with limited accuracy. The variation in geometric parameters, such as disc height, cross-sectional area of the intervertebral disc, size and position of the nucleus fiber orientation, or the number of fiber layers, can affect the mechanical behavior of the intervertebral disc and the whole lumbar functions [5, 6]. The procedure that joins FE models with different geometries might lead to remarkable different results and the modification in geometries and conditions of soft tissues in the finite element model introduced in previous biomechanical studies may alter the reported ROM.

6. Conclusions

We have presented a FE-model of the lumbar spine and have described how the model has been constructed based on the anatomical and computational features of the spine segments in the sake of computational efficiency. The intact model has been validated in good correlation with the literature where simulations have been achieved for physiological ROM (*Fig. 5*). This study presents a first step in the validation process of the FE-model for the individual human lumbar spine. Out of a number of model features analyzed computationally, reasonable approximations of the experimental data are provided by this model. Future work will focus on better understanding the sensitivity of FE predictions to variations in material properties associated with factors such as degeneration and the use of an optimization method based on differential evolution to calibrate the FE-model the whole lumbar spine. The approach for selecting such material properties involves calibrating the model by choosing the properties that produce the best compatibility with the in vivo and in vitro mechanical response of the lumbar spine. Whether, these approximations will be expressed terms of a FE-model for the intact L1–S1 finite element formulation, and the developed model could be considered as a valuable tool for the investigation of mechanical analysis of the lumbar segment in the perspective promote of pre and postoperative clinical analysis.

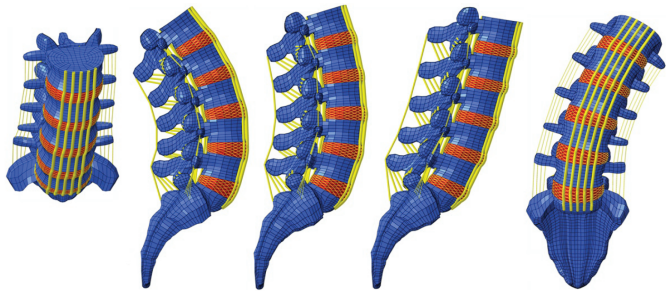

Fig. 5. Simulation of different Physiological Functions: 10 Nm + 100 N
5. ábra Szimulációs eredmények különböző fiziológiai hatásokra: 10 Nm + 100 N

References

[1] Panjabi M. M. – Krag M. H. – Chung T. Q. (1984): Effects of disc injury on mechanical behavior of the human spine. *Spine*, Vol. 9, pp. 707–713.

[2] Panjabi M. M. – Oxland T. R. – Yamamoto I. – Crisco J. J. (1994): Mechanical behavior of the human lumbar and lumbosacral spine as shown by three-dimensional load-displacement curves, *The Journal of Bone and Joint Surgery*, Series A, Vol. 76, pp. 413–424.

[3] Moramarco, V. – Palomar, A. P. – Pappalettere, C. – Doblaré, M. (2010): An accurate validation of a computational model of human lumbosacral segment, *Journal of Biomechanics*, Vol. 43, No, 2, pp. 334-342.

[4] Goel, V. K. – Monroe, B. T. – Gilbertson, L. G. – Brinckmann, P. (1995a): Interlaminar shear stresses and laminae separation in the disc. Finite element analysis of the L3-L4 motion segment subjected to axial compressive loads. *Spine*, Vol. 20, No. 6, pp. 689-698.

[5] Tyndyk M. A. – Barron V. – Mchugh P. E. – O'Mahoney D. (2007): Generation of a finite element model of the thoracolumbar spine, *Acta of Bioengineering and Biomechanics*, Vol. 9, pp. 35–46.

[6] Luoma K. – Riihimaki H. – Luukkonen R. et al. (2000): Low Back Pain in Relation to Lumbar Disc Degeneration. *Spine*, Vol. 25, No. 4, pp. 487-492.

[7] Natarajan R. N. – Andersson G. B. (1999): The influence of lumbar disc height and cross-sectional area on the mechanical response of the disc to physiologic loading. *Spine*, Vol. 24, pp. 1873–1881.

[8] Sheehan J. M. – C. I. Shaffrey – J. A. Jane (2001): Degenerative lumbar stenosis: The neurosurgical perspective. *Clinical Orthopaedics & Related Research*, Vol. 384, pp. 61-74.

[9] Patwardhan, A. G. et al. (1999): A Follower Load Increases the Load-Carrying Capacity of the Lumbar Spine in Compression. *Spine*, Vol. 24, No. 10, p. 1003.

[10] Zhong, Z. C. – Wei, S. H. – Wang, J. P. – Feng, C. K. – Chen, C. S. – Yu, C. H. (2006): Finite element analysis of the lumbar spine with a new cage using a topology optimization method, *Medical Engineering and Physics*, Vol. 28, No. 1, pp. 90-98.

[11] Rohlmann A. – Zander T. – Schmidt H. – Wilke H-J. – Bergmann G. (2006): Analysis of the influence of disc degeneration on the mechanicalbehavior of a lumbar motion segment using the finite element method. *Journal of Biomechanics*, Vol. 39, pp. 2484–2490. https://doi.org/10.1016/j.jbiomech.2005.07.026

[12] Schmidt H. – Heuer F. – Simon U. – Kettler A. – Rohlmann A. – Claes L. et al. (2006): Application of a new calibration method for a three-dimensional finite element model of a human lumbar annulus fibrosus. *Clinical Biomechanics*, Vol. 21, pp. 337–344.

[13] Park W. M. – Kim K. Y. – Kim H. (2013): Effects of degenerated intervertebral discs on intersegmental rotations, intradiscal pressures, and facet joint forces of the whole lumbar spine. *Computers in Biology and Medicine*, Vol. 43, pp. 1234–1240.

[14] Cao K. D. – Grimm M. J. – Yang K. H. (2001): Load sharing within a human lumbar vertebral body using the finite element method. *Spine*, Vol. 26, pp. 253–260.

[15] Moumene M. – Geisler F. H. (2007): Comparison of biomechanical function at ideal and varied surgical placement for two lumbar artificial disc implant designs: mobile-core versus fixed-core. *Spine*, Vol. 32, pp. 1840–1851. https://doi.org/10.1097/BRS.0b013e31811ec29c

[16] Langrana N. A. – Rodríguez J. (1995): Role of ligaments and facets in lumbar spinal stability. *Spine*, Vol. 20, pp. 887-900.

[17] Lu Y. M. – Hutton W. C. – Gharpuray V. M. (1996): Do bending, twisting, and diurnal fluid changes in the disc affect the propensity to prolapse? A viscoelastic finite element model. *Spine*, Vol. 21, pp. 2570–2579.

Ref.:
Bendoukha, Mohammed – **Mosbah,** Mustapha: *Biomechanical Evaluation of Lumbosacral Segments Response under Physiological Functions: Finite Element Analysis*
Építőanyag – Journal of Silicate Based and Composite Materials, Vol. 69, No. 3 (2017), 122–126. p.
https://doi.org/10.14382/epitoanyag-jsbcm.2017.22

On the deformation around holes described within a finite strain approach

Martin LEDERER ▪ Christian Doppler Laboratory for Lifetime and Reliability of Interfaces in Complex Multi-Material Electronics, TU Wien, Institute of Chemical Technologies and Analytics
Golta KHATIBI ▪ Christian Doppler Laboratory for Lifetime and Reliability of Interfaces in Complex Multi-Material Electronics, TU Wien, Institute of Chemical Technologies and Analytics
Érkezett: 2017. 11. 01. ▪ Received: 01. 11. 2017. ▪ https://doi.org/10.14382/epitoanyag-jsbcm.2017.23

Abstract
Numerous materials used in structural mechanics include a considerable amount of porosity. In order to assess their stability under load, it is necessary to evaluate the stress and strain concentrations around holes precisely. As a prerequisite for evaluations of stress distributions, an accurate definition of strain is required. For this purpose, we here propose logarithmic strain tensors in plane and spherical polar coordinates. It is demonstrated how the notion of incompressibility may accurately be described on the basis of a finite strain approach. Furthermore, the role of deviatoric and hydrostatic contributions to the stress is analyzed with respect to possible failure mechanisms.
Keywords: finite strain approach, material frame indifference, objectivity of a tensor, strain energy concentration
Kulcsszavak: véges nyúlások módszere, anyag nézőpont-függetlensége, tenzor objektivitás, alakváltozási energia koncentráció

Martin LEDERER
Dr. Martin Lederer is researcher at a Christian Doppler Laboratory at TU Wien. He has received his Ph.D. from the University of Vienna, where he is still teaching as a lecturer.

Golta KHATIBI
Dr. Golta Khatibi is head of the Christian Doppler Laboratory RELAB at TU Wien. She has authored over 100 scientific publications.

1. Introduction

It is a well known fact that accurate calculations of structural mechanics should be done in the frame of a finite strain approach considering all the nonlinear effects, which are relevant for the stability of a structure. Nevertheless, the linearized theory of elastic deformations is still widely used, because evaluations may be carried out straightforwardly within reasonable time. Furthermore, the predictions of the linear theory are usually expected to converge against exact results in the limit of small deformations. However, the performance of advanced computer simulations has substantially increased in recent years. Therefore, the possible issue of excessive computation time related to nonlinear evaluations has lost its significance. Consequently, it is here suggested that calculations of structural mechanics should nowadays be performed on the basis of a nonlinear theory.

In this context, we here give an example, where the predictions of finite strain theory may be evaluated analytically. It is demonstrated how the condition of incompressibility is perfectly fulfilled during integration of the equilibrium condition. For this purpose, the logarithmic strain, also called Hencky strain [1, 2], is expressed in polar coordinates in order to evaluate axisymmetric problems. Thereby, the material volume of an incompressible solid is precisely preserved. In contrast, the linear theory can only approximate such a behavior, whereby large deformations are accompanied by increasing deviations from exact results.

In this context it should be mentioned that the linearized strain violates the principle of Euclidean objectivity, which represents a prerequisite for the principle of material frame indifference [3]. According to material objectivity, the response of a material should be independent of the position of an observer in space and time. But the linearized strain tensor does not fulfil the requirements of an objective tensor. Such considerations are already known in the theory of finite strains. However, these problems are seldom treated in plane or spherical polar coordinates. It is therefore the aim of the present study, to extend the principles of finite strain theory to geometries, which are naturally described in polar coordinates.

2. Problem statement

In order to demonstrate some issues related to the linearized strain tensor, the classical solutions for a hole under uniform stress are briefly addressed here. Let us assume a pipe consisting of an isotropic, linear elastic material under internal and external hydrostatic pressure, as depicted in *Fig. 1*.

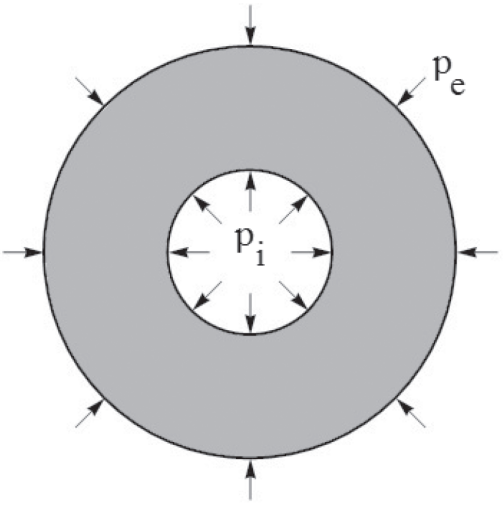

Fig. 1. A pipe under internal pressure p_i and external pressure p_e, schematically
1. ábra Nyomás alatt álló cső sémája; belső nyomás p_i és külső nyomás p_e

In his historical publication, *Lame* [4] applied polar coordinates to solve this axisymmetric problem. In the axisymmetric case, the equilibrium condition for the stress σ reads

$$\frac{\partial \sigma_{rr}}{\partial r} + \frac{\sigma_{rr} - \sigma_{\theta\theta}}{r} = 0 \quad (1),$$

where r denotes the radial and θ the circumferential direction. Further, axi-symmetry requires

$$\tau_{r\theta} = 0 \text{ (2a) and } \frac{\partial \sigma_{\theta\theta}}{\partial \theta} = 0 \quad (2b)$$

In this case, the linear strain tensor in polar coordinates writes as

$$\varepsilon_{rr} = \frac{\partial u}{\partial r},\ \varepsilon_{\theta\theta} = \frac{u}{r}, \text{ and } \varepsilon_{r\theta} = 0. \quad (3a\text{-}c)$$

Here, u are the displacements in radial direction. On the basis of Hooke's law one arrives at the equation

$$\frac{\partial^2 u}{\partial r^2} + \frac{1}{r}\frac{\partial u}{\partial r} - \frac{u}{r^2} = 0 \quad (4)$$

which is valid in both approximations, in plane strain as well as in plane stress. The general solution of this equation reads as

$$u(r) = C_1 \cdot r + \frac{C_2}{r} \quad (5)$$

where C_1 and C_2 are coefficients which are to be determined from boundary conditions. In the limit of large values for the outer radius of the pipe, the sample represents a hole in an infinite plate.

Let us now carry out the cross-check whether conservation of volume is fulfilled, when the solution given above is applied to incompressible materials: In plane strain approximation, the condition for volume-conserving, axisymmetric deformations may be expressed as

$$\varepsilon_{rr} + \varepsilon_{\theta\theta} = 0 \quad (6)$$

Inserting the definitions of (3 a, b) into (6) leads to the differential equation

$$\frac{\partial u}{\partial r} + \frac{u}{r} = 0 \quad (7)$$

This equation has the solution

$$u(r) = \frac{C_2}{r} \quad (8)$$

Consequently, the term including constant C_1 may be omitted in equation (5) when incompressible solids are considered. One now may check the change of volume described by deformation of the form (6). Let the inner and outer radius of the undeformed state be r_i and r_o, respectively. Assuming a normalized thickness of the plane strain model, the volume change ΔV during deformation according to (8) is

$$\Delta V = C_2^{\,2} \cdot \pi \cdot \left(\frac{1}{r_o} - \frac{1}{r_i} \right) \quad (9)$$

It is true that this result approaches 0 in the limit of infinitesimal deformations. But unfortunately, the result of equation (9) is not exactly zero!

3. Finite strain tensor in polar coordinates

Finite strain tensors are well described in the Lagrangian representation of continuum mechanics. The relation between the coordinates X_i of the deformed and the coordinates x_j of the initial configuration is in Cartesian coordinates defined by the deformation gradient tensor

$$F_{ij} = \frac{\partial X_i}{\partial x_j} \quad (10)$$

Here, it should be mentioned that the exact condition of incompressibility can be expressed as

$$\det(F) = 1. \quad (11)$$

From the deformation gradient, one obtains the Cauchy-Green tensor C through

$$C = F^T \cdot F \quad (12)$$

where F^T is the transposed matrix of F. Thus, the stretch tensor U may be derived from the relation

$$C = U^2 \quad (13)$$

The matrices C and U are both symmetric and have the same principal axes. Therefore, the stretch tensor U may also be expressed with the help of the outer product

$$U = \sum_a \sqrt{\lambda_a} \cdot \vec{r}_a \otimes \vec{r}_a, \quad (14)$$

where λ_a are the eigenvalues and $\vec{r}_a$ are the normalized eigenvectors of C, respectively. Now, there are several possibilities how finite strain tensors E may be defined with use of C or U. If one, however, likes to obtain a condition for incompressibility in the form of

$$tr(E) = 0, \quad (15)$$

where tr denotes the trace of a matrix, then the Hencky strain

$$E = \ln(U) \quad (16)$$

is the right choice. The Hencky strain is also called logarithmic strain. If one inserts (16) into (15), one gets a relation where the product of the sample dimensions remains constant, and this relation is equivalent to condition (11).

Let us now construct the equivalent expression in plane polar coordinates, whereby we here restrict ourselves to the axisymmetric case. Further, we here assume plane strain conditions. In consequence, we are left with two strain components pointing along orthogonal directions. By analogy to the Hencky strain one derives

$$E_{rr} = \ln\left(1 + \frac{\partial u}{\partial r}\right) \text{ and } E_{\theta\theta} = \ln\left(\frac{r+u}{r}\right) \quad (17\text{ a,b})$$

Moreover, a similar expression can be derived for spherical polar coordinates, where we have the coordinates r, θ and ϕ. For simplicity, we focus our interest on the case of uniform multiaxial stress around a spherical hole. Due to symmetry reasons, the strain components $E_{r\theta}$, $E_{r\phi}$ and $E_{q\phi}$ are zero. Thus, one obtains

$$E_{rr} = \ln\left(1 + \frac{\partial u}{\partial r}\right),\ E_{\theta\theta} = E_{\varphi\varphi} = \ln\left(\frac{r+u}{r}\right). \quad (18\text{ a-c})$$

Using the here mentioned strain tensors in plane or spherical polar coordinates together with the required symmetry conditions, one can express incompressibility of a material according to equation (15).

4. Integration of differential equations

We are now in the position to integrate the differential equations, which are obtained by inserting the logarithmic strain in polar coordinates into the incompressibility condition. In the case of plane strain, inserting of (17) into (15) yields

$$1+\frac{\partial u}{\partial r}=\frac{r}{u+r} \tag{19}$$

after simplification. The solution of this differential equation reads as

$$u(r)=\sqrt{r^2+a}-r \tag{20}$$

where the integration constant a is related to the amount of deformation. It is easily verified that a displacement field described by (20) preserves the volume of a body during deformation. Furthermore, a numerical similarity between the solutions (8) and (20) can be found for small values of a.

By analogy, the three-dimensional case of equation (18) may be evaluated. This time, one obtains the differential equation

$$1+\frac{\partial u}{\partial r}=\left(\frac{r}{u+r}\right)^2. \tag{21}$$

The solution of this equation reads as

$$u(r)=\sqrt[3]{r^3+b}-r, \tag{22}$$

where b denotes the integration constant. Like in the previous case, conservation of volume may easily be verified for this deformation mode.

It should be noticed that the solutions (20) and (22) are not restricted to purely elastic materials. Instead, they may also be applied to plastic deformations, but a detailed material model would be necessary to evaluate further details. Furthermore, the precise treatment of strain is also relevant for materials undergoing a volume change under hydrostatic pressure. In fact, many construction materials show a dependence of their strength on hydrostatic pressure, as for instance considered in the Drucker-Prager model [5] or its novel modifications [6]. In this context, the precise use of strain tensors is a prerequisite for implementation of such material models in computer simulations.

5. Solutions for elastic materials

Here, the solutions for isotropic, linear elastic materials are elaborated. Henceforth, compressible and incompressible materials are both included in the considerations. Further, we here at first consider the geometry and the loading case depicted in Fig. 1.

In view of the axisymmetric geometry investigated here, it appears convenient to rewrite the strain tensor

$$E=\begin{pmatrix} E_{rr} & 0 & 0 \\ 0 & E_{\theta\theta} & 0 \\ 0 & 0 & 0 \end{pmatrix} \tag{23}$$

in terms of deviatoric and hydrostatic strains:

$$E^{dev}=E-\frac{1}{3}tr(E)\cdot I \tag{24 a}$$

and

$$E^{hyd}=\frac{1}{3}tr(E)\cdot I, \tag{24 b}$$

where I is the 3-dimensional identity matrix. The corresponding deviatoric and hydrostatic stresses are:

$$\sigma^{dev}=\sigma-\frac{1}{3}tr(\sigma) \tag{25 a}$$

$$\sigma^{hyd}=\frac{1}{3}tr(\sigma)\cdot I \tag{25 b}$$

Per definition, the hydrostatic stress tensor is related to the pressure

$$p=-\frac{1}{3}tr(\sigma) \tag{26}$$

in the material. The orthogonal decomposition of stresses and strains permits the separation of material properties related to compression and shear:

For isotropic materials, two independent material parameters are needed. We use the bulk modulus K related to the volume change and the shear modulus G describing deviatoric deformations. When now Hooke's law is reformulated with use of the logarithmic strain, it is necessary to avoid a change of the material definitions. Hence, logarithmic strain components must, for the moment, be converted to their linearized amounts. This step is achieved according to the rules converting true strains E into linearized strains ε. Since

$$E=\ln(1+\varepsilon), \tag{27 a}$$

the inverse transformation writes

$$\varepsilon=\exp\{E\}-1. \tag{27 b}$$

Of course, it would also be possible to utilize some hyperelastic material law instead of keeping the definitions of a Hookean material. However, it is the purpose of the present investigation to study the effect of an improved strain definition without making changes to the material law.

Consequently, Hooke's law may be rewritten in the simple form

$$\sigma^{dev}=2G\cdot\left(\exp\{E^{dev}\}-I\right), \tag{28 a}$$

$$p=-K\cdot\left(\exp\{tr(E)\}-1\right). \tag{28 b}$$

In the context of finite strain theory, deviatoric and hydrostatic contributions to displacements may be considered in consecutive steps. The hydrostatic deformation mode is simply of the form $u=C_1\cdot r$. Inserting the coordinates of the hydrostatically deformed state as initial conditions into equation (20) yields

$$u(r) = \sqrt{(c+1)^2 \cdot r^2 + a} - r, \quad (29)$$

where the constants c and a are to be determined from the boundary conditions in combination with the material law. Here, it should be recognized that the intermediate transformation into a linearized strain according to (27 b) did not disturb the improvements achieved by use of the logarithmic strain.

By combination of the equations (23) through (29), the hydrostatic pressure inside the elastic material turns out to be

$$p = -K \cdot \left(2c + c^2\right) \quad (30)$$

We are now in the position to solve the boundary value problem

$$\sigma_{rr}(r_i) = -p_i \quad (31\text{ a})$$

and

$$\sigma_{rr}(r_o) = p_e, \quad (31\text{ b})$$

where p_i and p_e stand for the gas pressure at the inside and the outside of the pipe. One obtains the equations

$$-p_i = 2G\left(\frac{\sqrt[3]{c+1}^2 \cdot r_i}{\sqrt{(c+1)^2 r_i^2 + a}} - 1\right) + K\left(2c + c^2\right)$$

and

$$p_e = 2G\left(\frac{\sqrt[3]{c+1}^2 \cdot r_o}{\sqrt{(c+1)^2 r_o^2 + a}} - 1\right) + K\left(2c + c^2\right) \quad (32\text{ a, b})$$

for the constants c and a.

By analogy, one may also derive the solution for a spherical hole described by the strain tensor (18 a-c). Deviatoric and hydrostatic contributions to the strain take again the general form of equations (24 a, b). The same can be said about equations (25) through (28). The displacement field related to the spherical hole under hydrostatic pressure is

$$u(r) = \sqrt[3]{(c+1)^3 \cdot r^3 + b} - r \quad (33)$$

for isotropic elastic materials. For this geometry, the hydrostatic pressure inside the material reads as

$$p = -K\left(c^3 + 3c^2 + 3c\right) \quad (34)$$

The boundary value problem may again be formulated in the style of equation (31 a,b). Consequently, one derives

$$-p_i = 2G\left(\frac{(c+1)^2 \cdot r_i^2}{\sqrt[3]{(c+1)^3 r_i^3 + b}^2} - 1\right) + K\left(c^3 + 3c^2 + 3c\right) \quad (35\text{ a})$$

and

$$p_e = 2G\left(\frac{(c+1)^2 \cdot r_o^2}{\sqrt[3]{(c+1)^3 r_i^3 + b}^2} - 1\right) + K\left(c^3 + 3c^2 + 3c\right). \quad (35\text{ b})$$

The values for the constants a and c may be determined from this system of equations.

6. Concentration of strains around holes

Usually, the effect of the stress on a defect is discussed in terms of stress concentration factors. However, it has already been suggested to focus the interest rather on the increase of strain energy around a defect [7]. Indeed, strain energy concentration factors are not identical with stress concentration factors. The strain concentration strongly depends on the relation between the material parameters K and G. We will hereafter show that extremely high strain energy concentrations are found around holes in nearly incompressible materials. For this purpose, the orthogonal decomposition of stresses and strains into deviatoric and hydrostatic parts is once again utilized. Within the linearized approximation the strain energy density reads as

$$w = \frac{1}{2}\sigma : \varepsilon = \frac{1}{2}K \cdot tr(\varepsilon)^2 + G \cdot \varepsilon^{dev} : \varepsilon^{dev} \quad (36)$$

In the finite strain approach, it is necessary to consider the volume change aside from equations (28 a, b). Thus, one obtains

$$W = W^{hyd} + W^{dev} \quad (37\text{ a})$$

with

$$W^{hyd} = \int_V \frac{K}{2}\left(\exp\{tr(E) - 1\}^2\right) dV \quad (37\text{ b})$$

$$W^{dev} = \int_V G\left(\exp\{E^{dev}\} - I\right)^2 \cdot \exp\{tr(E)\} dV \quad (37\text{ c})$$

Let us now assume the geometry of a hole in an infinite plate under uniform biaxial tension in plane strain approximation. This means, we consider the geometry of Fig. 1 in the limit of $r_o \to \infty$. At the hole, the boundary condition writes as

$$\sigma_{rr} = 0. \quad (38)$$

In order to solve this boundary value problem, it should be recognized that the hydrostatic pressure is constant across the whole sample volume due to equation (30). Further, the radial components of hydrostatic and deviatoric stress tensor must be on balance at the inside of the hole. This means, the correlated radial components of equations (25 a and b) must compensate there:

$$\sigma_{rr} - \frac{1}{3}\left(\sigma_{rr} + \sigma_{\theta\theta} + \sigma_{zz}\right) = p \quad (39)$$

Considering the boundary condition (38) and $\sigma_{zz} = -p$, one derives

$$\sigma_{\theta\theta} = 2p \quad (40)$$

for the circumferential stress at the hole. In combination with equation (38) this leads to a stress concentration factor of $K_t = 2$ at the hole. On the other hand, the related deviatoric strain component at the hole may be written as

$$E_{rr}^{dev} = E_{rr} - \frac{1}{3}tr(E) \quad (42)$$

Consequently, the equation

$$\sigma_{rr}^{dev} = 2G \cdot \left(\exp\{E_{rr}^{dev}\} - 1\right) \quad (43)$$

holds. Let us now compare the strain $E_{rr}(\infty)$ far away from the hole with the strain $E_{rr}^{dev}(r_i)$ at the hole. Thus, one obtains

$$\frac{E_{rr}^{dev}(r_i)}{E_{rr}(\infty)} = \frac{\ln\left(1-\frac{p}{2G}\right)}{\frac{1}{2}\ln\left(1-\frac{p}{K}\right)} \tag{44}$$

In the limit for small deformations one obtains

$$\frac{E_{rr}^{dev}(r_i)}{E_{rr}(\infty)} \to \frac{K}{G}. \tag{45}$$

Now, it has become clear that the strain concentration factor depends on the ratio K/G of the material properties. Consequently, the strain energy (37) includes a term of this type.

The evaluations for the spherical hole can be derived by analogy. For nearly incompressible materials, extremely high concentrations of strain energy are found at the hole. For large strains, the correction of finite strain theory is governed by the relation between linear and logarithmic strains.

7. Discussion

The definition of strain is in principle independent of the materials described. However, a precise definition of material properties requires that the principle of material frame indifference is satisfied. An objective strain tensor must include an accurate description of the volume change in the material. In this respect, the linearized strain tensor leads to ambiguities, because it violates the principle of Euclidean objectivity. We have therefore used an objective strain tensor, which applies to axisymmetric problems. For this purpose, the logarithmic strain was formulated for polar coordinates. In this way, the material response to hydrostatic pressure could be described precisely. A separation of deviatoric and hydrostatic deformation modes was achieved on the basis of an orthogonal decomposition of stresses and strains. In conclusion, the concentrations of strain energy near holes could be evaluated.

Usually, evaluation methods derived from the linearized theory are justified in the sense that solutions are easy to calculate. In many applications, however, the solutions of structural mechanics are evaluated on numerical level. Since the efficiency of computer systems has enormously improved in recent years, the argument suggesting that the linearized strain was easy to compute has lost its relevance. In context with computer simulations, it is often of advantage to work with precise mathematical definitions, because of better convergence behavior observed for iterative algorithms.

Nevertheless, it must be said that in the limit of infinitesimal small deformations, the results of the present study agree with predictions of linear elasticity.

8. Summary and conclusions

The deformations around holes in isotropic elastic materials were evaluated in the frame of finite strain theory. The logarithmic strain tensor was applied to plane and to spherical polar coordinates, whereby axisymmetric geometries were considered. Owing to the symmetry of the problem, the equilibrium conditions simplified to ordinary differential equations, which could be solved straightforwardly. In consequence, the principle of material frame indifference was strictly fulfilled.

An interesting detail consists in the orthogonal decomposition of stresses and strains into deviatoric and hydrostatic parts. In this way the material properties related to shear modulus G and compression modulus K may be examined separately. In particular, a low value of the shear modulus G in comparison to the bulk modulus K can lead to tremendously high values of the strain energy due to large deviatoric strains near the hole.

The geometries considered here are very simple. On the other hand, analytical exact solutions are usually not derived for complex structures. Nevertheless, the methods developed here point the way how similar results can be obtained for structures of general shape. Moreover, the geometry of small holes inside a structure is of high relevance for materials with porosity. Insofar, our results apply to numerous materials used for structural mechanics.

9. Acknowledgements

The financial support of the Austrian Ministry of Science, Research and Economy and the National Foundation for Research, Technology and Development is gratefully acknowledged.

References

[1] H. Hencky (1925): Die Bewegungsgleichungen beim nicht-stationären Fließen plastischer Massen, *Zeitschrift f. technische Physik*, Vol. 9, pp. 215-220.

[2] H. Hencky (1929): Über die Form des Elastizitätsgesetzes bei ideal elastischen Stoffen, *Journal of Rheology*, Vol. 2, pp. 169-176.

[3] I-S. Liu (2004): On Euclidean objectivity and the principle of material frame-indifference, *Continuum Mechanics and Thermodynamics*, Vol. 16, pp. 177-183. https://doi.org/10.1007/s00161-003-0149-x

[4] G. Lame (1852): Lecons sur la theorie mathematque de l' elasticite, Paris: Bachelier

[5] D. C. Drucker – W. Prager (1952): Soil mechanics and plastic analysis or limit design. *Quarterly of Applied Mathematics*, Vol. 10, No. 2, pp. 157–165.

[6] L. H. Han – J. A. Elliott – A. C. Bentham – A. Mills – G. E. Amidon – B. C. Hancock (2008): A modified Drucker-Prager Cap model for die compaction simulation of pharmaceutical powders. *International Journal of Solids and Structures*, Vol. 45, pp. 3088-3106. https://doi.org/10.1016/j.ijsolstr.2008.01.024

[7] Z. Yang (2009): Stress and strain concentration factors for tension bars of circular cross-section with semicircular groove. *Engineering Fracture Mechanics*, Vol. 76, pp. 1683–1690. https://doi.org/10.1016/j.engfracmech.2009.03.005

Ref.:
Lederer, Martin – **Khatibi,** Golta: *On the deformation around holes described within a finite strain approach*
Építőanyag – Journal of Silicate Based and Composite Materials, Vol. 69, No. 3 (2017), 127–131. p.
https://doi.org/10.14382/epitoanyag-jsbcm.2017.23

Environment changes at the Ludlow and Pridoli boundary (Subpolar Urals)

Bronislav I. KANEV ▪ Dept. Of Ceramics and Silicate Engineering at Institute of Ceramics and Polymer Engineering, University of Miskolc ▪ slava.kanev.1995@mail.ru
Tatiana M. BEZNOSOVA ▪ Institute of Geology Komi SC UB RAS, Syktyvkar ▪ beznosova@geo.komisc.ru
Vladimir A. MATVEEV ▪ Institute of Geology Komi SC UB RAS, Syktyvkar ▪ vamatveev@geo.komisc.ru
László A. GÖMZE ▪ Dept. Of Ceramics and Silicate Engineering at Institute of Ceramics and Polymer Engineering, University of Miskolc ▪ femgomze@uni-miskolc.hu

Érkezett: 2017. 11. 04. ▪ Received: 04. 11. 2017. ▪ https://doi.org/10.14382/epitoanyag-jsbcm.2017.24

Abstract
The section of the Upper Silurian on the Western slope of the Subpolar Urals is located on the Kozhym River bank. This paper presents the results of studying of the geological structure of the upper Ludlowian section and data on lithology, geochemistry, and environment reconstructions of carbonate-terrigenous deposits of the late Ludlow and at the boundary of the Ludlow and Pridoli.
Keywords: environment, isotopes of carbonate carbon and oxygen, Ludlow, Pridoli, Sr/Ba ratio, Upper Silurian, Urals
Kulcsszavak: környezet, szén és oxigén izotópok, Ludlowi, Pridoli, Sr/Ba arány, késő Szilur

Bronislav I. KANEV
Graduated master's courses at the Syktyvkar State University named after P. Sorokin in the specialty Geology. In the process of studying in the magistracy the main fields of scientific interests were focused on conditions of formation of Upper Silurian deposits and association of Late Silurian benthic fauna on the Western slope of the Subpolar Urals. At present he is a PhD student at University of Miskolc under supervision of Prof. L. A. Gömze.

Tatiana M. BEZNOSOVA
Works at the N.P. Yushkin Institute of Geology, Komi Science Centre, Ural Division, Russian Academy of Sciences, Syktyvkar (Russian Federation). Author of 4 books and more than 150 articles.

Vladimir A. MATVEEV
Scientific employee in the laboratory of stratigraphy at the N.P. Yushkin Institute of Geology of the Komi SC UB RAS. Main fields of his research interest are stromatolite constructions of the Silurian of the Western slope of the Urals and the Chernov uplift. He is author of more than 30 scientific papers.

László A. GÖMZE
Establisher (in July 1st, 1999) of the Department of Ceramics and Silicate Engineering in the University of Miskolc, Hungary. Since then 7 students from the department have successfully completed their PhD theses and 4 of them were managed by Prof. Gömze. He is author or coauthor of 2 patents, 5 books and more than 250 scientific papers. Recently, he is the chair of the International Organization Board of ic-cmtp5 the 5th International Conference on Competitive Materials and Technological Processes (2018) and ic-rmm3 the 3rd International Conference on Rheology and Modeling of Materials (2017).

1. Introduction

In the regional stratigraphic scheme of the Urals adopted in 1991 the upper Ludlow on the investigated territory corresponds to the Sizim Regional Stage (= Ludfordian). The Lower Pridoli corresponds to the Belush'ya Regional Stage. The boundary of the Ludlow and Pridoli is established in the roof of the terrigenous-carbonate sequence [1, 2]. At the same time, there is another approach to determining the boundary between Ludlow and Pridioli [3].

This work is aimed to characterizing of the environment reconstruction of the boundary beds of the Sizim Regional Stage of Ludlow and Belush`ya Regional Stage of Pridoli.

The section of the boundary deposits of the Ludlow and Pridoli (section 236) is located on the left bank of the Kozhym River, in 700 m below the mouth of the Syv`yu River (*Fig. 1*).

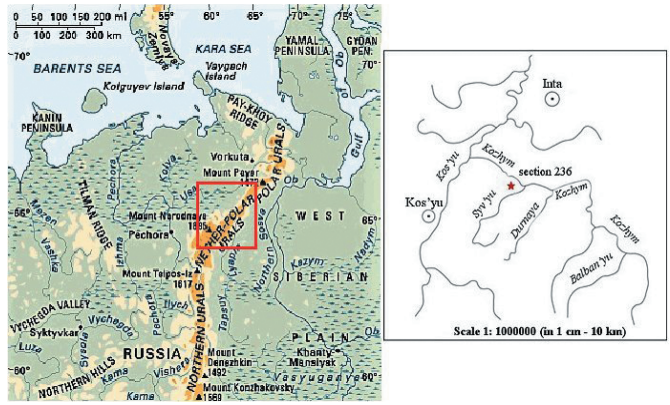

Fig.1. Scheme of the location of the studied section in the Kozhym river basin(latitude N65°40'0.86", longitude E59°45'2.09").
1. ábra A vizsgált szakasz helye a Kozhim-medencében (N65 ° 40'0.86 "szélesség, E59 ° 45'2.09" hosszúság).

2. Materials and methods

More than 80 samples of carbonate rocks have been studied to reconstruct the sedimentation environment of the Ludlow and Pridoli boundary deposits. Stratified sampling was conducted from all types of deposits transversely to stretch of rocks, every 50 cm. The barium and strontium contents were determined by the emission spectral analysis. Measurements of the stable isotopes ratios of carbon and oxygen ($\delta^{13}C$ and $\delta^{18}O$) are made with mass spectrometer «DELTA V Advantage». All analytical works were carried out at the N.P. Yushkin Institute of Geology of the Komi Scientific Centre of Ural Branch of Russian Academy of Sciences (in further: SC UB RAS).

3. Results and discussion

By the ratio Sr / Ba in sediments of the same age is possible to trace the transition from less saltwater sediments to normal marine, the Sr / Ba ratio of more than one indicates marine conditions, a ratio of less than one indicates a saltwater water environment. The increase in this ratio indicates an increase in salinity, and, conversely, it's lowering - the decrease in salinity [4, 5].

The distribution of the Sr / Ba ratio in the Upper Ludlow sediments is uneven with numerous deviations in the direction of increase and decrease, and varies from 0,57 to 30. The Sr / Ba ratio in the Lower Pridoli deposits varies from 1 to 7,9 (*Fig.*

2). Bearing in mind that most of the samples came from the boundary deposits of Ludlow and Pridioli showed a Sr / Ba ratio greater than one, it can be concluded that normal marine environment were in palaeobasin at the boundary of Ludlow and Pridoli.

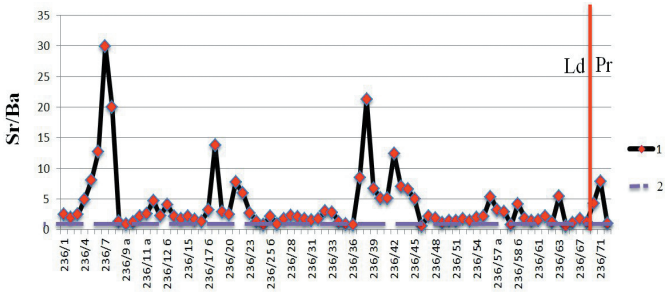

Fig. 2. Distribution of Sr-Ba values in the studied interval of the Ludlow and Pridoli sections – (1); the boundary between normal-marine and desalinated environments – (2).

2. ábra Az Sr-Ba értékek eloszlása a Ludlow és Pridoli szakaszok tanulmányozott intervallumában - (1); a normál tengeri és a sótalan környezet közötti határvonal - (2).

The concentration of strontium in the samples of the Upper Ludlow varies from 46 to 450 ppm is shown in *Fig. 3*. We must underline that the fault of this method can be obtained up to 27,7 – 30%. The Clarke' concentration of strontium in carbonate rocks by A.A. Beus is 610 ppm [6]. The study samples demonstrate lower Sr concentration. This is probably due to the fact that these carbonate deposits formed under conditions of hydrodynamic activity of water, at which strontium could be released [7, 8]. Such values indicate the penetration of freshwater in the basin [9].

The results of isotopic analysis of the boundary deposits of Ludlow and Pridoli are shown in graphs (*Figs. 3* and *4*). These results showed that none of the figurative points of distribution of $\delta^{13}C$ and $\delta^{18}O$ in the carbonate rocks of the Ludlow and Pridoli deposits did not fall within the range of the isotopic composition characteristic of the carbonate of normal sedimentary origin (*Fig. 4*). This probably indicates specific environment of sedimentation of these carbonate rocks.

The isotopic composition of carbon in the studied carbonate deposits of the upper Ludlow is characterized by a change in

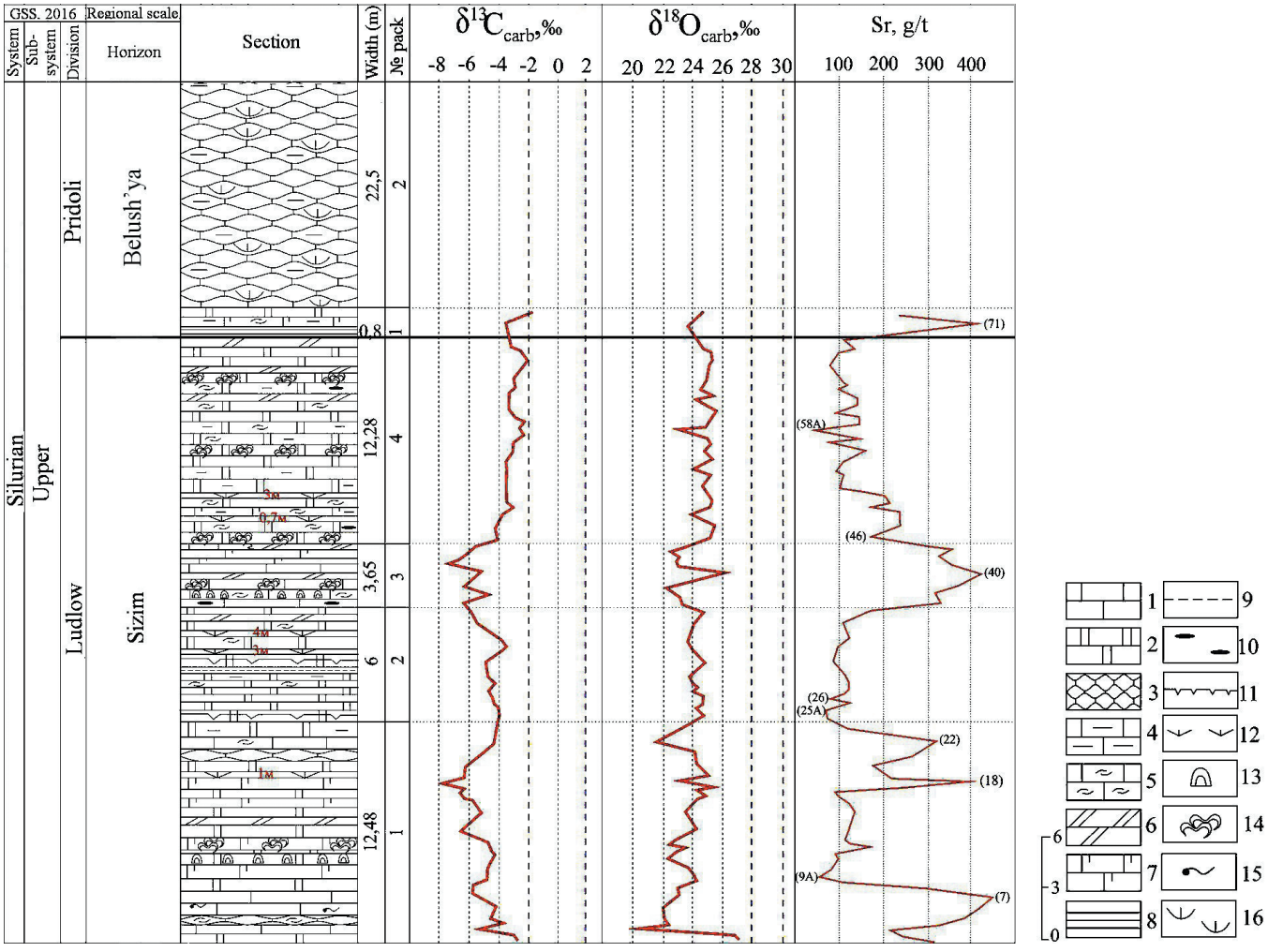

Fig. 3. The distribution of strontium, isotopes of carbonate carbon and oxygen in the boundary deposits of Ludlow and Pridoli on the Western slope of the Subpolar Urals (section 236). Legend: 1 – limestone; 2 – dolomite; 3 – limestone cloddy; 4 – limestone clayey; 5 – limestone detritus; 6 – marl; 7 – dolomitic limestone; 8 – argillite; 9 – clay; 10 – pebble; 11 – mud cracks; 12 – covered interval; 13 – stromatoporoids; 14 – stromatolites; 15 – burrows; 16 – brachiopod coquina.

3. ábra A stroncium, a karbonát-szén és az oxigén izotópjai az Urál-hegység szubpoláris nyugati lejtőjén a Ludlow és a Pridoli határövezetben (236. szakasz). Jelmagyarázat: 1 - mészkő; 2 - dolomit; 3 – rögös mészkő; 4 – agyagos mészkő; 5 – törmelékes mészkő; 6 - márga; 7 - dolomitikus mészkő; 8 - agyagpala; 9 - agyag; 10 - kavics; 11 - sár repedések; 12 - fedett intervallum; 13 – stromatolit poroidok; 14 - stromatolitok; 15 - zárványok; 16 - spirális coquina.

the value of $\delta^{13}C$ from -2,8‰ at the beginning, -7,8‰ closer to the middle part, then there is an increase in the values of $\delta^{13}C$ to -3,2‰ in the upper part of the studied section. At the same time, the value of $\delta^{18}O$ has a tendency to decrease from 27,1 to 20,4‰ in the lower part of the section, then there is a tendency to increase to 26,1‰ in the middle part. The upper part of the sequence demonstrates absence of significant changes in $\delta^{18}O$.

The isotopic composition of carbon and oxygen in the deposits of the Lower Pridoli are characterized by an increase in the values of $\delta^{13}C$ (from 3,6 to 1,7‰) and $\delta^{18}O$ (from 23,6 to 24,6‰).

In general, the boundary deposits of the Ludlow and Pridoli are characterized by lower values of $\delta^{13}C$ (from –2,1 to–7,8‰) compared with conventional marine carbonates (from –2 to 2‰) (*Fig. 3*). This probably indicates a sufficiently high bioproductivity in the basin [10].

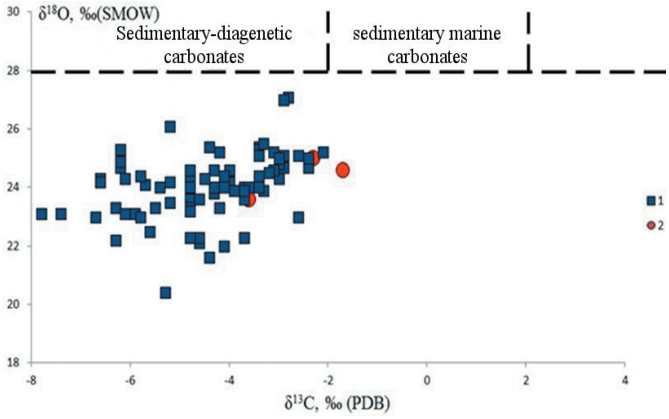

Fig. 4. Distribution of $\delta^{13}C$ and $\delta^{18}O$ in carbonate rocks of the Upper Ludlow and Lower Pridoli deposits: 1 - Ludlow deposits; 2 – Pridoli deposits.
4. ábra A δ13C és δ18O eloszlása a felső Ludlow és az alsó Pridoli karbonátos kőzetekben: 1 – Felső Ludlow; 2 – Alsó Pridoli

The isotopic composition of oxygen in the carbonate deposits of the upper Ludlow also has lower values of $\delta^{18}O$ (20,4 –27,1‰) compared with conventional marine carbonates (28 – 30‰) (*Figs. 3* and *4*). This may be a consequence of the influence of two factors: insignificant desalination and higher temperatures of paleobasin water. The fluctuation of the temperature gradient can be associated with the water circulation, and the change in the salinity of the water with the influx of fresh meteoric waters [8]. At the turn of the Ludlow and Pridoli there is a cardinal change in the composition of biota [11, 12].

4. Conclusion

Sedimentation in Ludlow occurred in a fairly bioproductive basin with a relative low sea level, slightly desalinated and with relatively high water temperatures.

Boundary deposits of the Ludlow and Pridoli were formed in environment of increased hydrodynamics with periodic influx of fresh water into the basin. Shallowing of the basin in the late Ludlow followed by transgression in the early Pridoli caused biotic turnover in the North Urals palaeobasin. The basin occupied the north-eastern margin of the Baltia palaeocontinent.

5. Acknowledgement

This work was supported by the Program of Fundamental Research of RAS "Biota in the geological history of the Timan-Severouralsk region: phylogenetics, evolution, paleecology and paleoclimate, biostratigraphy, stratigraphic geocorrelation" (project no. 115012130017).

References

[1] Matveev, V. A. – Kanev, B. I. (2016): Features of the upper Ludlow deposits in the silurian key section on the western slope of the Subpolar Urals. *Vestnik of Institute of Geology Komi SC UB RAS*. 2016. № 8 (260). pp. 3-8.
[2] Explanatory notes to the stratigraphical schemes of the Urals: Precambrian, Paleozoic. *Antsygin N. Ya.*, Ed., Yekaterinburg, 1994.
[3] Modzalevskaya, T. L. – Märss, T. (1991): On the age of the lower boundary of the Greben Regional Stage of the Urals. *Proceedings of the Estonian Academy of Sciences.* Geology, 1991. 40 (3), pp. 100–103.
[4] Katchenkov, S. M. (1959): Small chemical elements in sedimentary rocks and oils. – *Leningrad: Gostoptekhizdat, 1959.* – (Tr. VNIGRI, issue 143). - 271 p.
[5] Maslov, A. V. (2005): Sedimentary rocks: Methods of study and interpretation of obtained data: Textbook / Maslov A. V. Ekaterinburg: P*ublishing house of the USMU*, 2005. - 289 p.
[6] Perelman A. I. (1989): Geochemistry. *Moscow: Higher School*, 1989. - 528 p.
[7] Letnikova, E. F. (2005): Geochemical specificity of carbonate deposits of various geodynamic settings of the northeastern segment of the Paleo-Asiatic Ocean. *Litosfera = Lithosphere*, 2005. - No. 1. pp. 70-81.
[8] Yudovich, Ya. E. (1981): Regional geochemistry of sedimentary strata. Leningrad, Nauka, 1981, 276 p.
[9] Yudovich, Ya. E. – Ketris, M. P. (2011): Geochemical indicators of lithogenesis (lithological geochemistry). *Syktyvkar: Geoprint*. 2011. 742 p.
[10] Nurgalieva, N. G. (2005): Relationship between carbon and oxygen isotopes in carbonate rocks in the eastern Russian Plate. *Uchen. Zap. KGU. Estestven. Nauki*, 2005, vol. 147. part 3. pp. 38–48.
[11] Beznosova, T. M. (2008): Brachiopod communities and biostratigraphy of Upper Ordovician, Silurian and Lower Devonian of the north-eastern margin of Baltica Palaeocontinent. *Ekaterinburg*. UrO RAN, 2008. 218 p.
[12] Beznosova, T. M. – Matveev, V. A. – Sokolova, L. V. – Kanev B. I. (2017): Regional manifestation of the global Ludford event (Lau Event) in the section of the Western slope of the Subpolar Urals. *Geodynamics, substance, ore genesis of the East European Platform and its folded framing: Extended abstract of scientific conference reports*. Syktyvkar: IG Komi SC UB RAS, 2017. pp. 19-21.

Ref.:
Kanev, Bronislav I. – **Beznosova,** Tatiana M. – **Matveev,** Vladimir A. – **Gömze,** László A.: *Environment changes at the Ludlow and Pridoli boundary (Subpolar Urals)*
Építőanyag – Journal of Silicate Based and Composite Materials, Vol. 69, No. 3 (2017), 132–134. p.
https://doi.org/10.14382/epitoanyag-jsbcm.2017.24

Környezetváltozás a Ludlowi és Pridoli korok határán (sarkvidéki Ural)
A szerzők által vizsgált és jelen munkában bemutatott Felső-Silurian szakasz az Urál-hegység sarkköri (Subpoláris) részének nyugati lejtőjén található, a Kozhim folyó partján. Ez a tanulmány bemutatja a Ludlow felső szakasz geológiai felépítésének szerkezetét, valamint vizsgálati adatokat a késő Ludlow illetve a Ludlow és a Pridoli határában található szárazföldi karbonát lelőhelyek litológiájára, geokémiájára és környezeti rekonstrukciójára vonatkozóan.